IOWA STATE UNIVERSITY
Digital Repository

Graduate Theses and Dissertations | Graduate College

2009

Control approach to high-speed large-range AFM imaging and nanofabrication

Yan Yan
Iowa State University

Follow this and additional works at: http://lib.dr.iastate.edu/etd

 Part of the Mechanical Engineering Commons

Recommended Citation
Yan, Yan, "Control approach to high-speed large-range AFM imaging and nanofabrication" (2009). *Graduate Theses and Dissertations*. 10618.
http://lib.dr.iastate.edu/etd/10618

This Thesis is brought to you for free and open access by the Graduate College at Iowa State University Digital Repository. It has been accepted for inclusion in Graduate Theses and Dissertations by an authorized administrator of Iowa State University Digital Repository. For more information, please contact digirep@iastate.edu.

Control approach to high-speed large-range AFM imaging and nanofabrication

by

Yan Yan

A thesis submitted to the graduate faculty

in partial fulfillment of the requirements for the degree of

MASTER OF SCIENCE

Major: Mechanical Engineering

Program of Study Committee:
Qingze Zou, Major Professor
Atul Kelkar
Xinwei Wang

Iowa State University

Ames, Iowa

2009

Copyright © Yan Yan, 2009. All rights reserved.

DEDICATION

I would like to dedicate this thesis to my parents. Without their love and support I would not have been able to complete this work.

TABLE OF CONTENTS

LIST OF TABLES

LIST OF FIGURES

ACKNOWLEDGEMENTS

I would like to express my deep and sincere gratitude to my advisor, Dr. Qingze Zou. His wide knowledge and novel ideas inspired and advised me to finish this work. His understanding, encouragement and guidance have provided me a strong support throughout the study. Moreover, his attitude toward research and logical way of thinking have had a remarkable impact on my entire career. With his advise, this study has become enjoyable and meaningful.

I would also like to thank my committee members for their efforts and contributions to this work: Dr. Atul Kelkar and Dr. Xinwei Wang.

I am deeply grateful to my lab colleagues. Without their knowledge, experience and assistance this work would not have been successful.

I would like to acknowledge NSF Grants CMMI 0626417 and DUE 0632908 for the financial support for my study and work.

Finally, I would like to present my special gratitude to my dear parents and friends. Their loving support makes me feel strong, independent and confident.

ABSTRACT

In this thesis, two inversion-based feedforward control approaches have been developed and implemented to high-speed large-range atomic force microscope (AFM) imaging and nanofabrication, respectively. High-speed large-range AFM imaging and nanofabrication are needed in many areas and have attracted great interests. Challenges, however, must be overcome because in high-speed large-range AFM operation, large positioning error of the AFM probe relative to the sample can be generated due to the adverse effects of the hardware. The nonlinear hysteresis and the vibrational dynamics effects of the piezotube actuator must be addressed during the high-speed lateral scanning of the AFM imaging over large imaging size. In addition, precision positioning of the AFM probe in the vertical direction is even more challenging (than the lateral scanning) because the desired trajectory (i.e., the sample topography profile) is unknown in general, and the probe positioning is also effected by and sensitive to the probe-sample interaction. Finally, in AFM multi-axis nanofabrication, additional positioning errors are induced by the large cross-axis dynamics coupling effect. The large positioning errors generated during high-speed, large-range fabrication will lead to large defects in the fabricated structures or devices. In the thesis, firstly, to compensate for the adverse effects generated during high-speed large-range AFM imaging, an integrated approach is proposed, which combines the enhanced inversion-based iterative control technique (EIIC) for lateral x-y axis scanning with a dual-stage piezoactuator for the vertical z-axis positioning. The main contribution of this integrated approach is the combination of an advanced control algorithm with an advanced hardware platform. This approach is demonstrated in experiments by imaging a large-size (50 μm) calibration sample at high speed (50 Hz scan rate). Then secondly, to achieve high-speed large-range multi-axis AFM nanofabrication, a recently developed model-less inversion-based iterative control technique (MIIC) is utilized to overcome the adverse effects involved in high-speed large-range multi-axis AFM nanofabrication. By using this advanced control technique,

the adverse effects can be effectively accounted for and precision positioning control can be achieved in all $x-y-z$ axes. This approach is illustrated experimentally by implementing it to fabricate large-size ($\sim$50 μm) pentagram patterns via mechanical scratching on a gold-coated silicon sample surface at high speed ($\sim$4.5 mm s^{-1}).

CHAPTER 1. INTRODUCTION

Owing to its great potentials for fast imaging with nanoscale spatial resolution and high-throughput nanofabrication, high-speed large-range atomic force microscope (AFM) technology has drawn the attention of not only the scientific community, but also the industry. This technology requires the precision positioning of the probe relative to the sample, and thereby, is confronted by the challenge—maintaining precision (probe-to-sample) positioning in high-speed, large-range operation.

During the high-speed lateral scanning of the AFM imaging, the nonlinear hysteresis and the vibrational dynamics effects of the piezotube actuator can induce large positioning errors and large imaging distortion can be generated. In addition, vertical precision positioning of the AFM probe during the imaging process is even more challenging (than lateral scanning). This is because the desired trajectory (i.e., the sample topography profile) is unknown in general, and the probe positioning is also effected by and sensitive to the probe-sample interaction. Large positioning errors of the AFM probe can result in not only the damage of the probe (when the sample is hard) or the sample (when the sample is soft), but also large imaging distortion. Thus, it is critical to maintain the precision positioning of the probe relative to the sample in both lateral and vertical directions during high-speed, large-range AFM imaging.

Moreover, the motion control in AFM probe-based nanofabrication can be more demanding, because unlike AFM imaging where the motion in one axis is substantially slower than that in other axes, the motion in each $x-y-z$ axis can be at high speed, and positioning errors in different axes can be superimposed during nanofabrication, leading to large distortions in the final structure/device fabricated. Additionally, when the fabrication speed is high and/or the operation range is large, the cross-axis dynamics coupling of piezo actuators (1) can become large, resulting in large fabrication distortions as well. Therefore, it is important to maintain the precision positioning of the probe relative to the sample

in all x-y-z axes during high-speed, large-range AFM probe-based nanofabrication.

In this thesis, two inversion-based feedforward control approaches have been developed and implemented to high-speed large-range AFM imaging and nanofabrication. To compensate for the adverse effects generated during high-speed large-range AFM imaging, an integrated approach is proposed, which combines the enhanced inversion-based iterative control (EIIC) technique (2) for the lateral x-y scanning, along with a dual-stage piezo actuator for the vertical z-axis positioning of the AFM-probe. Besides, for high-speed, large-range AFM probe-based nanofabrication, a model-less inversion-based iterative control technique (MIIC) (3) is utilized to compensate for the dynamics-coupling effect in multi-axis motions, as well as to account for the hysteresis and the dynamics effects in the motion of each individual x, y and z axis. By using these control approaches, the adverse effects can be effectively accounted for and precision positioning control can be achieved in both lateral and vertical directions. The implementations of the integrated approach and the MIIC approach are illustrated through experiments.

1.1 High-speed Large-range AFM operation

The Atomic force microscope (AFM), invented by Binnig, Quate, and Gerber (4) in 1980s, is one of the most versatile tools of the visualization and measurement of surface features with nanometer sized dimensions. The AFM can reach the resolution of fractions of a nanometer, more than 1000 times better than the optical diffraction limit, which cannot be achieved by using conventional optical microscopes. Also compared to the scanning electron microscope (SEM), the AFM provides a true three-dimensional surface profile and samples viewed by AFM do not require any special treatments (such as metal/carbon coatings) that would irreversibly change or damage the sample. On the other hand, the AFM is confronted by some disadvantages—the limited image size, relatively low scan rate, and creep, hysteresis, and vibration dynamics effects of the piezo actuator (5) as well as the cross-talk between the $x-y-z$ axes, which makes high-speed large-range AFM imaging challenging. However, AFM imaging in high speed, large range or both is needed in areas including material science and engineering (6; 7), biomedical imaging (8; 9), and nanoscale metrology in industry. For instance, AFM imaging of living cells takes a few to tens of minutes (8). If the sample properties change rapidly during

that time, the resulting AFM images can contain substantial distortions (i.e., temporal errors) because the initial pixel and the final pixel of the image are acquired at different time instants during the slow scanning (10). AFM is also used as a key tool for nanoscale metrology in industries such as hard-disk drive and semiconductor. However, current AFM is too slow to meet the demanded inspection throughput at over 100 wafers/hour (which is over 2 orders higher than the throughput achievable on the current AFM). Moreover, in these applications (e.g., the imaging of rapid biological processes like the migration of living cell (8), or the wafer examination in semiconductor industry), relatively large-size imaging range is also needed (e.g., the cell size at $\sim 100\ \mu m$ is close to the full displacement range of the piezo actuator). Evidently, there exist needs to achieve high-speed, large-size AFM imaging.

In addition to its well-known capabilities in imaging, the AFM-based technology has become increasingly popular in the fabrication of nanoscale structures due to its low cost and great technical potential. Current probe-based nanofabrication processes (11)-(15), however, are limited by the low-throughput of the process, which, in turn, hurdles their practical implementations. Although such a low-throughput can be improved through hardware improvements such as parallel probes (15), the throughput is eventually constrained by the relatively low rate and limited displacement range. Thus, it is important to achieve the AFM probe-based nanofabrication during high-speed large-range motion.

1.2 Inversion-based Iterative Control Approach

Iterative learning control (ILC) is based on the notion that the performance of a system that executes the same task multiple times can be improved by learning from previous executions (trials, iterations, passes) (16). This approach is attractive for AFM lateral scanning and nanofabrication because the desired motion is *repetitive*, and the desired trajectory is pre-specified (usually a triangle trajectory). Therefore, it is possible to utilize the tracking results of the entire trajectory (e.g., one period of triangle trajectory) from last iteration to generate the control input at current time instant, rather than generating the control input only based on the tracking prior to the current time instant—as in feedback control. In other words, ILC approach provides the possibility to explore the noncausalityto enhance output tracking. Particularly, it is shown recently that the use of noncausality is one of the main advantages of ILC approach over feedback approach in tracking periodic trajectories (17). We note that piezo

actuators tend to have nonminimum-phase characteristics in their dynamics (18; 19), and it is well-known that exact output tracking of nonminimum-phase systems can not be achieved by using feedback control alone (20). Such tracking limits, however, can be eliminated by utilizing noncausality in output tracking, as in the stable-inversion technique (21) and its extension in the ILC framework (1; 22). Thus, it is advantageous to use inversion-based iterative control technique to achieve high-speed large-range AFM lateral scanning and nanofabrication. In this thesis, two recently-developed ILC techniques, which are the enhanced inversion-based iterative control (EIIC) and the model-less inversion-based iterative control (MIIC) are utilized in the AFM lateral scanning and nanofabrication, respectively.

1.3 Thesis overview

In the rest of the thesis, the control approaches to achieve high-speed large-range AFM imaging and nanofabrication are illustrated in Chapter 2 and 3, respectively. Each chapter is self-contained.

Chapter 2 is devoted to the development of the integrated approach to high-speed large-range AFM imaging. First, we describe the control issues related to AFM imaging. Then the integrated approach is proposed, which combines the enhanced inversion-based iterative control (EIIC) technique (2) for the lateral x-y scanning, along with a dual-stage piezo actuator for the vertical z-axis positioning of the AFM-probe. There we described the EIIC technique and the dual-stage piezo actuator in detail. After that the proposed method is demonstrated in experiments by imaging a large-size (50 μ m) calibration sample at high speed (50 Hz scan rate), where the experimental results are presented and discussed.

Chapter 3 addresses the control approach to high-speed large-range AFM probe-based nanofabrication. First, we briefly review the probe-based nanofabrication methods, and the challenges in precision positioning control of the probe relative to the sample during high-speed large-range motion. Then the MIIC method is presented, and the coupling-compensation process by using the MIIC is described. After that, this approach is illustrated experimentally by implementing it to fabricate large-size ($\sim$50 μm) pentagram patterns via mechanical scratching on a gold-coated silicon sample surface at high speed ($\sim$4.5 mm s^{-1}). It is followed by the experimental results and discussion.

Finally, our conclusions are given in Chapter 4.

CHAPTER 2. AN INTEGRATED APPROACH TO PIEZO-ACTUATOR POSITIONING IN HIGH-SPEED AFM IMAGING

2.1 Introduction

In this paper, we propose an integrated approach to achieve high-speed imaging of large-size samples on the atomic force microscope (AFM). The proposed approach combines the enhanced inversion-based iterative control (EIIC) technique (2) for the lateral x-y scanning, along with a dual-stage piezo actuator for the vertical z-axis positioning of the AFM-probe. High-speed, large-size AFM imaging is challenging because the precision positioning of the AFM probe relative to the sample in all x, y, z-axes must be achieved. However, due to the adverse effects—the nonlinear hysteresis and the linear vibrational dynamics effects—of the piezotube actuator (5; 22), large positioning errors of the AFM probe relative to the sample can occur during high-speed, large-size lateral x-y axes scanning (22; 23; 1). Moreover, the vertical z-axis precision positioning of the AFM probe (during high-speed imaging) is further limited by issues such as the desired trajectory (i.e., the sample topography profile) is unknown in general, and the probe positioning is sensitive to the probe-sample interaction (24). Large positioning errors of the AFM probe can result in the damage of the probe (when the sample is hard) (25), or the sample (when the sample is soft) (26). Therefore, it is important to maintain the precision positioning of the AFM probe relative to the sample during high-speed, large-size AFM imaging.

High-speed AFM imaging is needed in areas including material science and engineering (6; 7), biomedical imaging (8; 9), and nanoscale metrology in industry. For instance, AFM imaging of living cells may take tens of minutes (8). If the sample properties change rapidly during that time, the resulting AFM images can contain substantial distortions (i.e., temporal errors) because the initial pixel and the final pixel of the image are acquired at different time instants during the slow scanning (10). AFM

is also used as a key tool for nanoscale metrology in industries such as hard-disk drive and semiconductor. However, current AFM is too slow to meet the demanded inspection throughput at over 100 wafers/hour (which is over 2 order higher than the throughput achievable on current AFM). Moreover, in these applications (e.g., the imaging of rapid biological processes like the migration of living cell (8), or the wafer examination in semiconductor industry), relatively large-size imaging range is also needed (e.g., the cell size at $\sim 100\ \mu m$ is close to the full displacement range of the piezo actuator). Evidently, there exist needs to develop high-speed, large-size AFM imaging.

High-speed, large-size AFM imaging is challenging. We note that significant improvement in AFM imaging has been achieved through the hardware improvements such as the high-bandwidth piezo actuators (27; 28; 29), the small cantilevers(30; 31), the improved positioning structure (32), and the high-speed data acquisition system (32). By using high-bandwidth piezo actuators (around two orders higher than the piezo actuators used on commercial AFMs), the imaging speed of AFM can be significantly increased (around two orders faster) (27; 28). However, high-bandwidth piezo actuators also tend to have much smaller displacement range. As a result, the imaging size of such high-speed AFMs is rather small (around 1$\sim$5 μm, compared to the imaging size of $\sim$100 μm on commercial AFMs), and only flat samples with small aspect ratio ($<$ 100 nm) can be imaged (compared to the vertical positioning range of $\sim$6 μm on commercial AFMs). Thus such an approach of using high-bandwidth piezo actuators alone can not achieve both high-speed and large size AFM imaging. To maintain the large imaging size (in both lateral and vertical directions) during high-speed AFM operation, the adverse vibrational dynamics (of the piezo actuator and the cantilever) and hysteresis (of the piezo actuator) effects must be addressed (33). Recently, advanced control techniques, such as the robust control techniques (19; 23) and the inversion-based feedforward control techniques (5; 34; 35) have been developed to account for these adverse vibrations in AFM imaging. Particularly, it has been demonstrated that the inversion-based iterative control technique (1; 22; 2) is highly efficient in compensating for both the vibrational dynamics and the hysteresis effect during lateral scanning operation. Compensating for these two adverse effects in the vertical direction, however, is much more challenging, because the desired trajectory to follow (i.e., the sample profile) is unknown and non-periodic in general, large dynamics

uncertainty can exist due to the probe variations, and the nonlinear effect of the tip-sample interaction (24). Therefore, there exists a need to develop new approach to achieve high-speed, large-size AFM imaging.

The contribution of this article is the development of an integrated approach. The proposed approach utilizes the recently developed EIIC approach (2) to compensate for both the hysteresis and vibrational dynamics effects of piezo actuators in lateral scanning, as well as takes advantage of a dual-stage piezo actuator for vertical positioning of the AFM probe. The proposed approach is demonstrated in experiments, and the experimental results show that high-speed precision lateral scanning at large size scanning (50 μm) can be achieved by using the EIIC technique. Combined with the dual-stage piezoactuator, such high-speed scanning significantly improved the imaging speed than commercial AFMs. Therefore, the proposed integrated approach presents a very promising approach to achieve high-speed AFM imaging.

2.2 Integrated Approach to High-Speed Large-Size AFM Imaging

In this section, the integrated approach to high-speed large-size AFM imaging is presented. We start with briefly describing the AFM imaging process.

2.2.1 AFM Imaging

The AFM system utilizes piezo actuators to position the AFM probe in both lateral x-y axes and vertical z-axis (Fig. 3.1). Various AFM operation modes have been developed to image sample topography or to measure sample properties (36). For example, in the contact-force mode imaging, the AFM probe scans over the sample under a raster pattern (see Fig. 3.1). The feedback controller of the piezo actuator for the vertical z-axis is used to maintain the cantilever deflection around a set point value (which corresponds to a constant tip-sample interaction force). The deflection of the cantilever is sensed using optical detection and utilized as the feedback signal in the z-axis feedback control. As discussed in the introduction, precision positioning of the AFM-probe relative to the sample in all x-y-z axes is critical to ensure the imaging/measurement precision, as well as to avoid potential damage of

the sample and/or the probe during high-speed, large-size AFM imaging. Next, we present the EIIC algorithm to achieve the high-speed lateral *x*-*y* axes scanning, and then the dual-stage piezo actuator for the vertical *z*-axis precision positioning during high-speed AFM imaging.

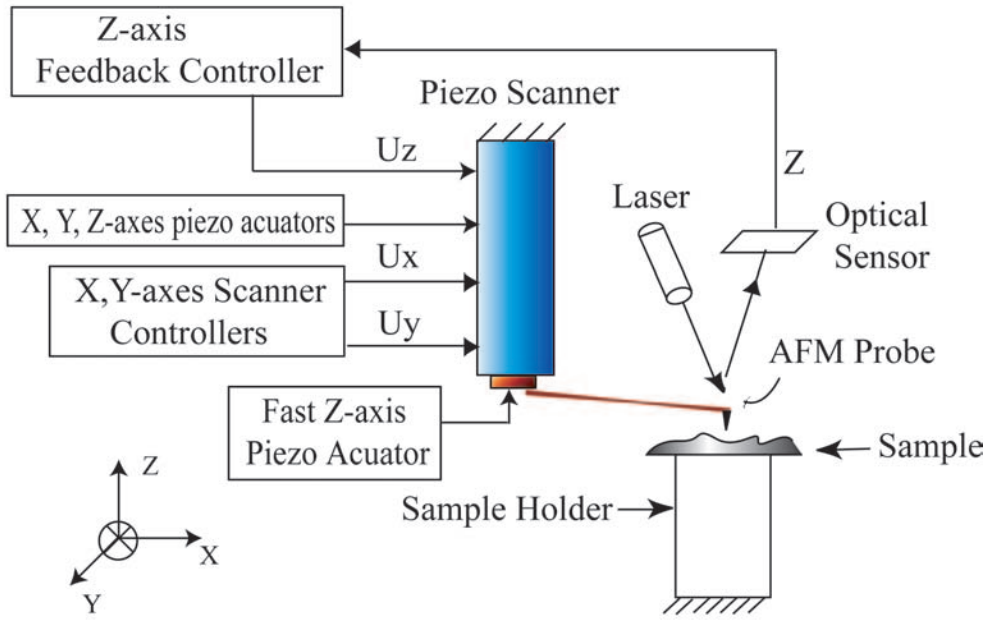

Figure 2.1 The schematic diagram of AFM operation.

2.2.2 Enhanced Inversion-based Iterative Control (EIIC) for Lateral Scanning

We propose to use a novel iterative control technique to achieve high-speed, large-size precision positioning in lateral *x*-*y* axes scanning. Iterative learning control (ILC) approach is attractive for lateral scanning because the desired motion during lateral scanning is repetitive, and the desired trajectory is pre-specified (usually a triangle trajectory). Therefore, it is possible to utilize the tracking results of the entire trajectory (e.g., one period of triangle trajectory) from last iteration to generate the control input at current time instant, rather than generating the control input only based on the tracking prior to the current time instant—as in feedback control. In other words, ILC approach provides the possibility

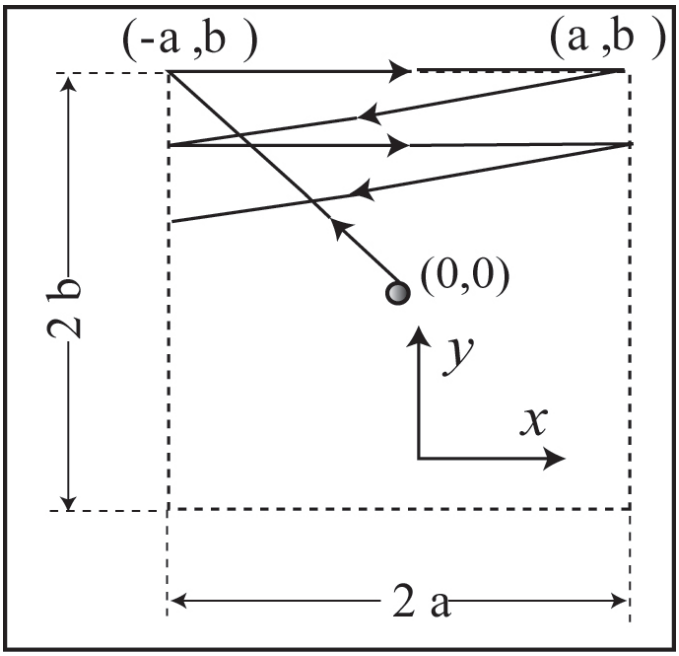

Figure 2.2 Top view of the typical scanning trajectories for AFM imaging.

to explore the noncausality to enhance output tracking. Particularly, it is shown recently that the use of noncausality is one of the main advantages of ILC approach over feedback approach in tracking periodic trajectories (17). We note that piezo actuators tend to have nonminimum-phase characteristics in their dynamics (18; 19), and it is well-known that exact output tracking of nonminimum-phase systems can not be achieved by using feedback control alone (20). Such tracking limits, however, can be eliminated by utilizing noncausality in output tracking, as in the stable-inversion technique (21) and its extension in the ILC framework (1; 22). Thus, it is advantageous to use inversion-based iterative control technique to achieve high-speed lateral scanning.

The EIIC control law is described in frequency domain as follows

$$\begin{aligned} u_0(j\omega) &= G^{-1}(j\omega)x_d(j\omega), \\ |u_{k+1}(j\omega)| &= |u_k(j\omega)| + \rho(\omega)|G^{-1}(j\omega)|[|x_d(j\omega)| - |x_k(j\omega)|],\ k \geq 1, \\ \angle u_{k+1}(j\omega) &= \angle u_k(j\omega) + (\angle x_d(j\omega) - \angle x_k(j\omega)),\ k \geq 1. \end{aligned} \tag{2.1}$$

In the above Eqs. (1, 2), $G(j\omega)$ is the model of the system's frequency response, $\rho(\omega)$ is a frequency-

dependent positive iterative coefficient, $x_d(j\omega)$ is the Fourier transform of the desired output, and $u_k(j\omega)$ and $x_k(j\omega)$ are the Fourier transform of the input and the output from the k^{th} iteration, respectively (see Fig. 2.3). It can be shown that the above EIIC algorithm will lead to precision tracking of the frequency component of the desired trajectory $x_d(j\omega)$ at frequency ω provided that 1) the iterative coefficient $\rho(\omega)$ is properly chosen, and 2) the noise/disturbance at that frequency is small enough. Specifically, we consider there exists measurement noise or disturbance $x_{\mathcal{N}}(t)$ added to the linear response of the system $x_k(t)$, resulting in the measured system response $\hat{x}(t)$ as

$$\hat{x}_k(t) \;=\; x_k(t) + x_N(t), \tag{2.2}$$

then it can be shown (2) that precision tracking at frequency ω can be achieved by using the EIIC algorithm if and only if the iterative coefficient $\rho(\omega)$ is chosen as

$$0 < \rho(\omega) < \rho_{sup}(\omega) \triangleq \frac{2}{|\Delta G(j\omega)|}, \tag{2.3}$$

where $\Delta G(j\omega)$ is the dynamics uncertainty described as the ratio of the actual system dynamics $G(j\omega)$ with respect to its model $G_m(j\omega)$, i.e.,

$$\Delta G(j\omega) = \frac{G(j\omega)}{G_m(j\omega)} = \frac{|G(j\omega)|e^{j\angle G(\omega)}}{|G_m(j\omega)|e^{j\angle G_m(\omega)}} \triangleq |\Delta G(j\omega)|e^{j\Delta\angle G(j\omega)}. \tag{2.4}$$

Thus, for the measurement noise that is bounded by a frequency-dependent constant $\varepsilon(\omega)$, $|x_N(j\omega)| \leq \varepsilon(\omega)$, the error in the output tracking is bounded as

$$\begin{aligned} \lim_{k\to\infty} |\hat{x}_k(j\omega) - x_d(j\omega)| \quad &\leq \quad 2\varepsilon(\omega), \\ |\angle x_k(j\omega) - \angle x_d(j\omega)| \quad &\leq \quad \tan^{-1}\frac{\varepsilon(\omega)}{|x_d(j\omega)|},\ for\ k \geq 1. \end{aligned} \tag{2.5}$$

The above Eq. (2.5) shows that at frequency ω, precision tracking can be achieved if the noise/disturbance is small (i.e., $\varepsilon(\omega)$ is small). Therefore, Equation (2.5) can be used as a guideline in practice to determine whether or not the EIIC input should be applied—the EIIC algorithm should be applied at frequencies ω where the signal-to-noise ratio is large enough. Otherwise, we set the control input to zero at that frequency ω. Such an implementation scheme implies that the EIIC algorithm will lead to precision tracking of a modified desired trajectory which equals to the original desired trajectory at frequencies where the EIIC law is applied. Note that to implement the EIIC algorithm, the system

dynamics uncertainty needs be estimated first (see Eq. (2.4)), from which the iterative coefficient $\rho(\omega)$ can be determined (Eq. (2.3)). In practice, the system uncertainty $\Delta G(j\omega)$ can be estimated experimentally, for example, through the measurement of the frequency responses under various conditions (e.g., under different input levels and at different initial locations), and the power spectrum of the system noise can also be experimentally measured. Moreover, the effect of the measurement noise on the output tracking can be significantly reduced by using averaged result in the EIIC algorithm (3). These implementation related issues are illustrated in the experimental example next.

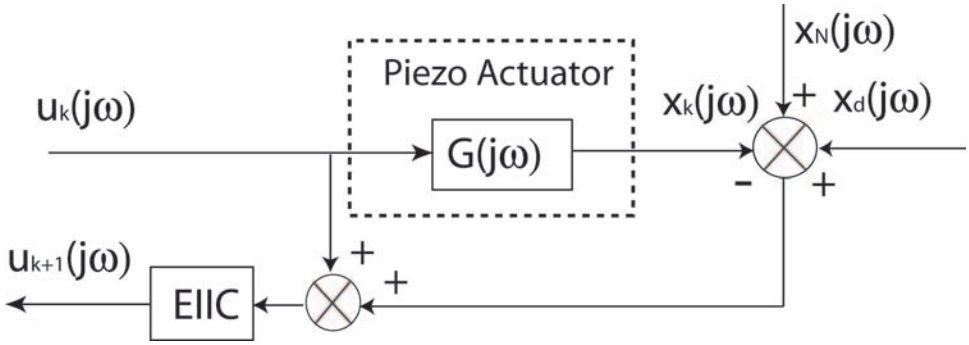

Figure 2.3 Block diagram of the EIIC algorithm.

2.2.3 Dual-stage Piezo Actuator for Vertical Positioning of AFM-Probe

Next, a novel dual-stage piezo actuator is utilized to achieve vertical z-axis precision positioning at high-speed (see Fig. 3.1). In the state-of-the-art commercial AFMs, a piezotube actuator with relatively large displacement range ($\sim$6 μm) is used for vertical z-axis positioning. Large displacement range is needed in order to accurately measure the sample topography at various aspect ratios (both large and small). However, piezo actuators with large displacement and large output force (i.e., stress, needed to drive the AFM probe and the associated mechanical linkage) also tends to have large mass, which results in relatively small bandwidth of the actuator, limiting the precision positioning to the low-speed range. Recently, advanced control techniques (18; 19; 37) have been developed to significantly improve the positioning precision of piezo actuators at high-speed for AFM imaging. The positioning speed of piezo actuators, however, is ultimately limited by their bandwidth. Thus, the dual-stage piezo actuator

provides a promising alternative approach to achieve high-speed, large-range precision positioning.

The proposed dual-stage piezo actuator consists of a large-range, low-bandwidth piezotube actuator (as used in commercial AFMs) and a small-range, high-bandwidth piezo stack actuator. The small piezo stack actuator is attached to the end of the large piezotube actuator and directly acts on the cantilever (as depicted in Fig. 3.1). The large-range piezo actuator has a displacement range of $\sim$6 μm and an open-loop bandwidth $\sim$2.4 kHz, while the small-range piezo actuator has a displacement range of $\sim$1 μm and a much higher open-loop bandwidth (over 20 times higher). Therefore, with the integration of these two actuators, the dual-stage piezo actuator can possess both large displacement range and high bandwidth, which in turn, allows precision positioning in much higher speed motion than the piezotube actuator on commercial AFM.

The dual-stage piezo actuator is controlled by using feedback control. In general, the feedback control of dual-stage actuators can be configured in two different approaches: the feedback control loop of the fast piezo actuator can be 1) nested with, or 2) in parallel to the feedback loop of the slow piezo actuator. In the proposed dual-stage piezo actuator, a nested feedback control system is employed (see Fig. 2.4), where relatively high-frequency but small-amplitude frequency components in the error signal are compensated for mainly by the fast piezo actuator, while those relatively low-frequency but large-amplitude frequency components are accounted for mainly by the slow piezo actuator. Therefore, the dual-stage actuator can position the probe rapidly in the vertical direction to follow sample profile of large variations. As the first step, proportional-integral (PI) controllers were used to control both the slow z and the fast z actuators in this article for ease of implementation and robustness of the control system. Advanced control techniques (18; 19; 37) can be integrated with the proposed dual-stage actuator to further improve the z-axis positioning.

2.3 Experimental Results and Discussion

In this section, we illustrate the proposed approach by implementing it to AFM imaging in experiments. The goal is to demonstrate that the AFM imaging speed of large size samples can be significantly

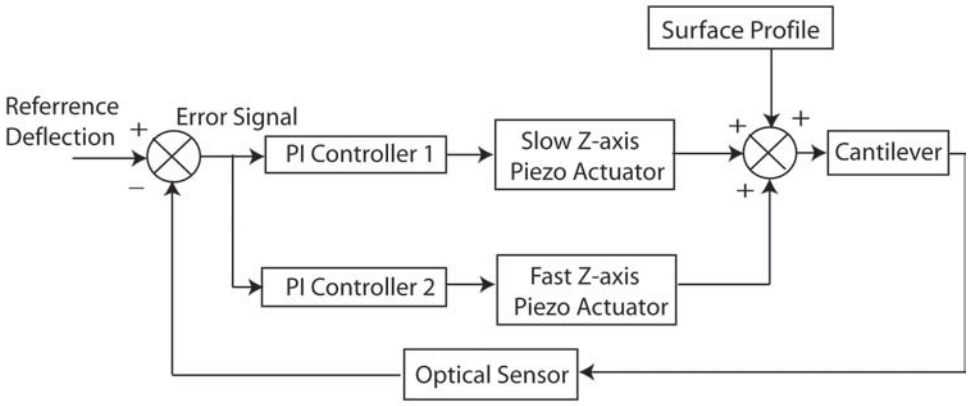

Figure 2.4 The feedback control loop of the dual-stage piezo actuator.

increased by using the proposed approach. We start with briefly describing the experimental system.

2.3.1 Experimental Setup.

The AFM system (*Dimension*^{TM} 3100, Veeco Inc) studied in this article utilizes piezotube actuators to position the AFM probe with respect to the sample during the imaging in all *x*-*y*-*z* axes. All the control inputs were generated by using MATLAB-xPC-target (Mathworks, Inc.) and sent through a data acquisition card (DAQ) to the high-voltage amplifier of the AFM-controller—the PID-control circuit of the AFM controller was bypassed (See Fig. 2.5).

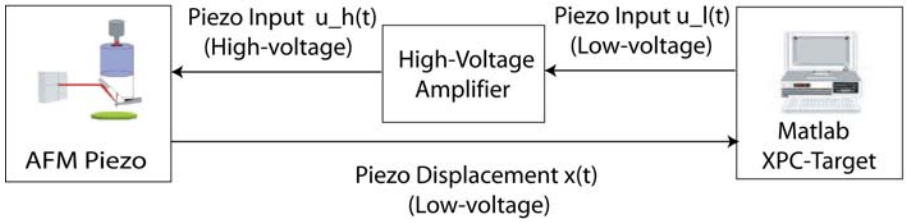

Figure 2.5 The experimental setup block diagram.

2.3.2 Experimental Tracking Results in Lateral X-axis Scanning.

The EIIC algorithm was applied to the control of x-axis lateral scanning with large imaging size (50 μm). The desired trajectory was a triangle trajectory—as usually used in AFM imaging. The output tracking at five different scan rates (5 Hz, 10 Hz, 50 Hz, 100 Hz, 200 Hz) were evaluated in experiments by comparing them to those obtained by using the DC-gain method and proportional-integral (PI) feedback controller. In the DC-gain method, the control input was generated by scaling the desired output with the DC gain of the piezo actuator. The DC-gain method does not account for the hysteresis nor the vibrational dynamics effects, thereby the tracking results obtained by the DC-gain method quantitatively demonstrate the adverse effects of the hysteresis and/or the vibrational dynamics effects on output tracking. The PI feedback control (or PID-type of feedback control in general) is widely used in commercial AFM systems. The following PI feedback controller was used in this experiment

$$G_{PI}(s) \;=\; \frac{a\times k_p}{s+a}+\frac{b\times k_i}{s+b}, \tag{2.6}$$

where k_p and k_i are the proportional and the integral gain, respectively. Note that a low-pass filter $1/(s+a)$ was added to the PI controller to reduce the signal noise effect, where $a=b=200\ \pi$, and the PI parameters k_p and k_i were tuned in experiments to enhance the control performance of the PI controller while maintaining the stability of the closed-loop system. Particularly, $k_p=1.2$, and $k_i=50$ were chosen for the scan rates of 5 Hz, 10 Hz and 50 Hz. For higher scan rates of 100 Hz and 200 Hz, the proportional gain was reduced to $k_p=0.8$ (for 100 Hz) or $k_p=0.6$ (for 200 Hz). In addition, the following notch filter was added before the application of the PI controller to increase the gain margin of the system, which, in turn, increased the bandwidth of the closed-loop system. (35). The transfer function of the notch filter $G_\ell(s)$ is

$$G_\ell(s) \;=\; \frac{s^2+613s+3.758\times 10^7}{s^2+12260s+3.758\times 10^7}\ , \tag{2.7}$$

and the total PI feedback controller became

$$G_c(s) \;=\; G_{PI}(s)\times G_\ell(s). \tag{2.8}$$

The dynamics of the AFM system from x-axis piezo actuator input voltage to the x-axis output was modeled experimentally using a dynamic signal analyzer (DSA) (Hewlett Packard 356653A). A

sinusoidal input voltage generated by the DSA was applied to the piezo actuator through a power amplifier, and the x-axis sensor output voltage of the actuator was measured (using an inductive sensor) and fed back to the DSA to construct the frequency responses. To quantify the dynamics uncertainties, the frequency responses were measured under three different driven input levels (20 mv, 40 mv, and 60 mV) at three different locations (by offsetting the initial position of the piezotube actuator). The measured frequency responses are shown in Fig. 2.6 for the frequency range $\omega \in [0,\ 2]$ kHz. The iterative coefficient $\rho(\omega)$ of the EIIC approach is determined according to Eq. (2.3), and is shown in Fig. 2.7. The lateral tracking results by using the EIIC technique with those by using the DC-gain method and the PI controller at the four different scan rates (10Hz, 50 Hz, 100 Hz, and 200 Hz) are compared in Fig. 3.7. The tracking errors are also compared in Table. 2.1, where the maximum tracking error E_M, the RMS error E_{RMS}, and the relative RMS error $E_{RMS}(\%)$ are defined as

$$\begin{aligned} E_M &\triangleq \frac{\|y_d(\cdot)-y_k(\cdot)\|_\infty}{\|y_d(\cdot)\|_\infty}, \\ E_{RMS} &\triangleq \frac{\|y_d(\cdot)-y_k(\cdot)\|_2}{\|y_d(\cdot)\|_2}, \\ E_{RMS}(\%) &\triangleq \frac{\|y_d(\cdot)-y_k(\cdot)\|_2}{\|y_d(\cdot)\|_2} \times 100\%. \end{aligned} \tag{2.9}$$

The experimental results demonstrate that precision positioning can be achieved by using the EIIC algorithm in large-range, high-speed scanning. For the scan size of 50 μm used in the experiments, the hysteresis effect was significant, resulting in large positioning error. As shown in Fig. 3.7 (a1) and (a2), the hysteresis-caused tracking error $E_{RMS}(\%)$ reached almost 15% of the total displacement range when the scan rate was slow at 10 Hz (see the tracking result obtained by using the DC-gain method). Such large tracking error was reduced by using the PI feedback controller to 2.72% (see Table 2.1), which was mainly caused by phase-delay. The small phase-delay-caused tracking error was further reduced by using the EIIC algorithm—the RMS tracking error E_{RMS} of the EIIC algorithm tracking was reduced to $\sim$0.04 μm (0.16% of the total displacement range). As the scan rate increased to 50 Hz, the vibrational dynamics effect was augmented to the hysteresis effect, resulting in even larger tracking errors (see Fig. 3.7 and Table 2.1). However, precision tracking was still maintained when using the EIIC approach—the RMS tracking error is only 0.11 μm, about 2.5% of that when using the PI control (see Fig. 3.7 (b1) and (b2)). Even when the scan rate was increased to 200 Hz, the tracking error of using

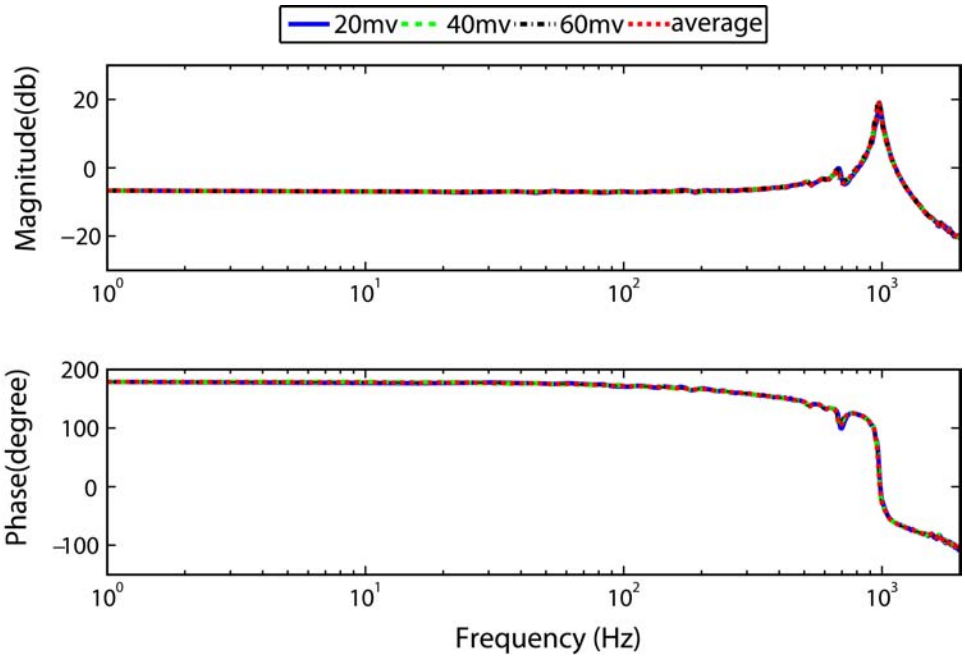

Figure 2.6 The experimentally measured frequency responses of the x-axis piezo actuator on the AFM at three different input amplitude levels (20 mv, 40 mv, and 60 mv), with comparison to the averaged frequency response.

the EIIC approach was still small (only about 3.4% of that by using the PI control, or about 10% of that by using the DC-gain method (see Fig. 3.7 (d1) and (d2)). Thus, the EIIC algorithm can effectively account for both the hysteresis and vibrational dynamics effects during highs-speed, large-size lateral scanning.

Due to the vertical z-axis bandwidth limit (the bandwidth of the vertical z-axis positioning needs to be much higher than that in the lateral scanning), scanning speed up to 50 Hz was used in the following AFM imaging experiments. However, we note that with the development of advanced control techniques for vertical z-axis positioning (18; 19; 37), the control system bandwidth of the dual-stage z-axis piezo actuator can be further improved.

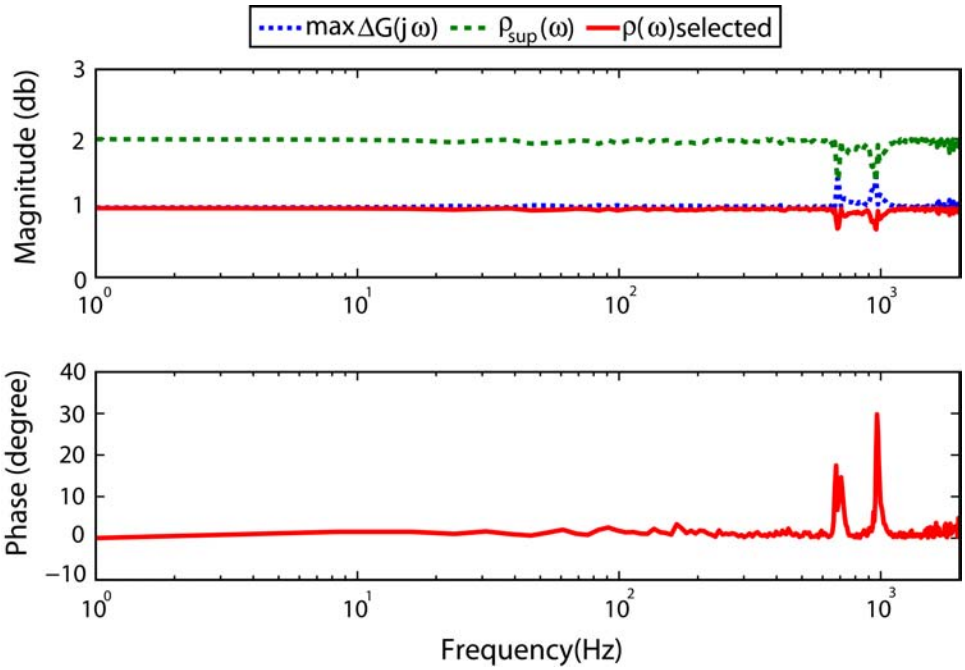

Figure 2.7 The measured magnitude variation of the piezo actuator (see Eq. (2.4)), the upper bound of the iterative coefficient $\rho_{sup}(\omega)$, and the iterative coefficient $\rho(\omega)$ used in the experiments; and the measured phase variation.

2.3.3 AFM Image Results and Discussion

Next, the proposed integrated approach was applied to AFM imaging under the contact force mode. A standard silicon calibration sample with nominal square pitches of 200 nm height and 5 μm length and width was imaged in the experiments. The following three different sets of experiments were conducted: 1). To evaluate the imaging improvement gained from the EIIC technique, the EIIC technique and the PI controller were used, respectively, for the lateral x-y axis scanning, and the dual-stage piezo actuator was used for the z-axis positioning in both cases. The obtained images are compared in Fig. 2.9 for the scan rate of 10 Hz ((a1) and (b1)) and 50 Hz ((a2) and (b2)), respectively. 2) To evaluate the z-axis positioning improvement gained from the use of the dual-stage actuator, the sample was imaged by using the dual-stage piezo actuator and by using the conventional piezotube actuator (called single-stage piezo actuator in the following), respectively, for the z-axis AFM-probe positioning. The converged EIIC input obtained above was applied for the lateral $x-y$ axes scanning in both cases. The

Table 2.1 Comparison of the tracking errors obtained by using the DC-gain method, the PI controller, and the EIIC approach at different scan rates.

Scan Rate	$E_M(\mu m)$			$E_{RMS}(\mu m)$			$\hat{E}_{RMS}(\%)$		
(Hz)	**DC-gain**	**PI**	**EIIC**	**DC-gain**	**PI**	**EIIC**	**DC-gain**	**PI**	**EIIC**
5	4.87	0.77	0.12	3.53	0.41	0.03	14.12	1.64	0.12
10	4.93	1.20	0.15	3.57	0.68	0.04	14.28	2.72	0.16
50	5.46	4.64	0.68	3.93	4.13	0.11	15.72	16.52	0.44
100	6.91	7.91	1.13	4.76	5.03	0.24	19.04	20.12	0.96
200	9.70	19.32	1.86	5.15	14.12	0.46	20.60	56.48	1.84

obtained images are compared in Fig. 2.10 for the scan rates of 10 Hz ((a1) and (b1)) and 50 Hz ((a2) and (b2)). The cross-section plots obtained by using these two different z-axis piezo actuators are also compared in Fig. 2.11 for the scan rate of 10 Hz ((a1) and (b1)) and 50 Hz ((a2) and (b2)), respectively. 3). Finally, to evaluate the entire imaging improvement gained from the integrated approach, the EIIC technique was applied (for lateral scanning) along with the dual-stage piezo actuator (for the vertical probe positioning) during the imaging. Then the obtained images at two different scan rates (10 Hz and 50 Hz) were compared with the images obtained by using the single-stage piezo actuator (for vertical positioning) along with a) the DC-gain method, or b) the PI controller (for lateral scanning), respectively. The obtained imaging results are shown in Fig. 2.12.

Imaging Improvement Gained from EIIC Approach The comparison of the experimental imaging results obtained by using the EIIC technique with those obtained by using the PI controller—for the lateral scanning—shows that the EIIC technique effectively removed the image distortion caused by the hysteresis and dynamics effects of piezo actuator (Note in both cases, the dual-stage piezo actuator was used for the probe positioning in the vertical direction). When the imaging speed was relatively slow at 10 Hz, the PI controller can track the triangle scanning trajectory relatively well, and the imaging distortion was also small. As shown in Fig. 2.9 (a1), the size of the pitches are almost the same as the nominal size. When the imaging speed was increased to 50 Hz, much larger tracking error occurred in the lateral scanning with the PI controller (see Fig. 3.7 (b2)), which led to larger image distortion. As shown in Fig. 2.9 (a2), the width of the pitches in each column varied significantly: the width of

the pitches in the first column is $\sim$3 μm, while the width of the pitches in second column is more than doubled at $\sim$7 μm. On the contrary, precision tracking was still achieved at this high-speed, large-range scanning when using the EIIC algorithm (see Fig. 2.9 (b2)), and the maximum difference among the width of pitches is less than 0.5 μm. Therefore, the experimental imaging results demonstrate that the use of the EIIC approach for the lateral scanning can significantly remove the distortions in AFM image generated at high-speed .

Precision positioning of dual-stage actuator over single-stage actuator As shown in Fig. 2.10 (a1) and (b1), at relatively low imaging speed (scan rate of 10 Hz), the single-stage piezo actuator can track the sample topography relatively well, and the cross-section view of image obtained (see Fig. 2.11 (a1)) reveals that the imaged height of the sample is close to the nominal height of the sample at 200 nm, however, the edge of the pitch was still not as sharp as that obtained by using the dual-stage piezo actuator (compare Fig. 2.10 (a1) with (b1)), and the cross-section view of the image obtained by using the dual-stage actuator shows much smaller upper oscillations (on average) than that obtained by using the single-stage actuator (compare Fig. 2.11 (a1) with (b1)). When the image speed increased to 50 Hz, much larger AFM-probe oscillations were generated when using the single-stage actuator, resulting in large image distortions (see Fig. 2.10 (a2)). Such large image distortions can also be seen from the cross-section view in Fig. 2.11 (a2): the measured depth-width of the sample topography has large variations in the peak values (from the nominal of 200 nm by 5 μ m) and became triangle shape—away from the nominal square shape. On the contrary, the dual-stage actuator can track the sample topography much better at this high-speed imaging: the image obtained in Fig. 2.10 (b2), clearly shows the square pitches of the calibration sample, which is quite close to the image obtained at low speed. In addition, the cross-section view of the image (Fig. 2.11 (b2)) shows that the sample depth-width measured by using the dual-stage actuator is much closer to the nominal sample depth-width. Therefore, the experimental results show that the dual-stage piezo can enhance the vertical z-axis precision positioning of the AFM probe during high-speed AFM imaging.

High-speed imaging improvement with the integrated approach The image comparison among the proposed integrated method (using the EIIC approach for lateral scanning along with the dual-

stage piezo actuator for vertical positioning), the current commercial method (PI feedback controller for lateral scanning along with single-stage piezo actuator for vertical positioning), and the previous commercial method (DC-gain method for lateral scanning along with single-stage piezo actuator for vertical positioning) is shown in Fig. 2.12. By using the previous commercial method, when the scan rate was 10 Hz (see in Fig. 2.12 (a1)), the variations among the width and the length of the pitches were pronounced (the width of the pitches in the first column is $\sim$6 μm, while the width of the pitches in the last column is $\sim$3 μm, and the length of pitches in the first row is $\sim$3 μm, while the length of pitches in the last row is $\sim$6 μm), indicating large tracking errors in both x and y axes. When the scan rate increased, such imaging distortions caused by lateral x-y axes positioning error become even larger (see Fig. 2.12 (a2)). Moreover, the variation of the pitches depth also became significant (the pitches in the first column are much darker than those in other columns in Fig. 2.12 (a2)), indicating large vertical z-axis positioning errors. By using the current commercial method, the imaging quality was significantly improved at relatively low imaging speed: the imaging distortion caused by lateral positioning error was effectively removed at the scan rate of 10 Hz (compare Fig. 2.12 (a1) with (b1)). However, large imaging distortions still exist at high-speed imaging (50 Hz). On the contrary, by using the proposed integrated approach, imaging quality was significantly improved. At high-speed (50 Hz) imaging, the edge of pitches is sharper than that obtained by the other two methods at much lower speed 10 Hz imaging (Compare Fig. 2.12 (c2) with Fig. 2.12 (a1) and (b1)), and the large variations of the pitch width and the pitch depth appearing in the other two methods were also effectively removed (Compare Fig. 2.12 (c2) with (a2) and (b2)). As a result, the image obtained at how speed is quite close to that obtained at low speed. Therefore, the experimental results demonstrate that AFM imaging speed can be significantly improved by using the proposed integrated approach.

2.4 Conclusion

An integrated approach to achieve high-speed AFM imaging of large-size samples is proposed. The approach combines the enhanced inversion-based iterative control (EIIC) technique for lateral x-y axes scanning with a dual-stage piezo actuator for vertical z-axis positioning. The EIIC algorithm can effectively compensate for the nonlinear hysteresis and vibrational dynamics effects of piezo actuator

during high-speed, large-size lateral scanning. The dual-stage actuator combines a large-size piezo actuator of relatively low bandwidth with a small-size piezo actuator of high bandwidth, resulting in high-speed positioning at large displacement range. The proposed approach was demonstrated by implementing it to image a large size (50 μm) calibration sample at high-speed (50 Hz scan rate). The experimental results illustrated the efficacy of the proposed integrated approach in achieving high-speed large-range AFM imaging.

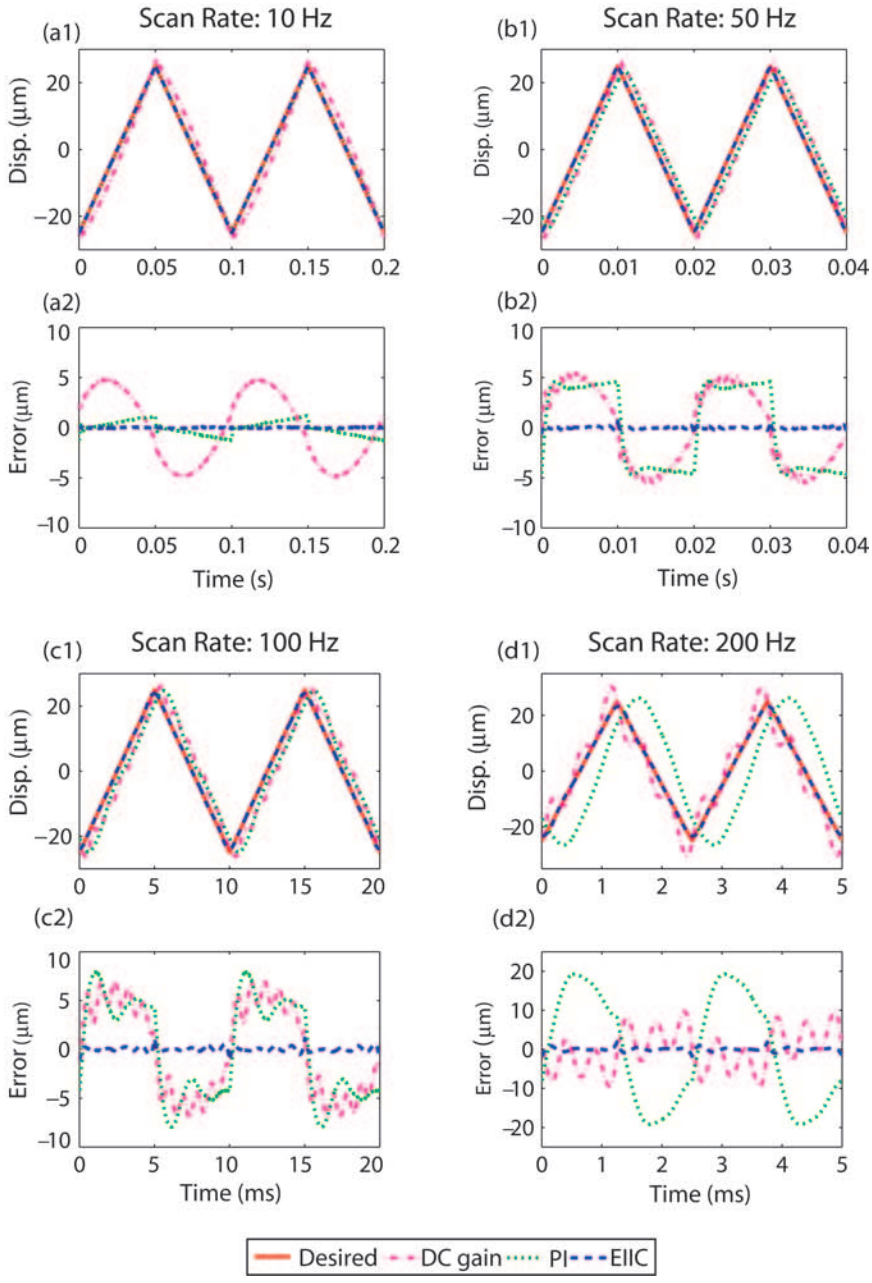

Figure 2.8 Comparison of the lateral tracking results by using the EIIC technique with that by using the DC-gain method and the PI controller at 10 Hz (a1), 50 Hz (b1), 100 Hz (c1), and 200 Hz (d2), and the comparison of the corresponding tracking errors at these four different scan rates ((a2), (b2), (c2), and (d2), respectively).

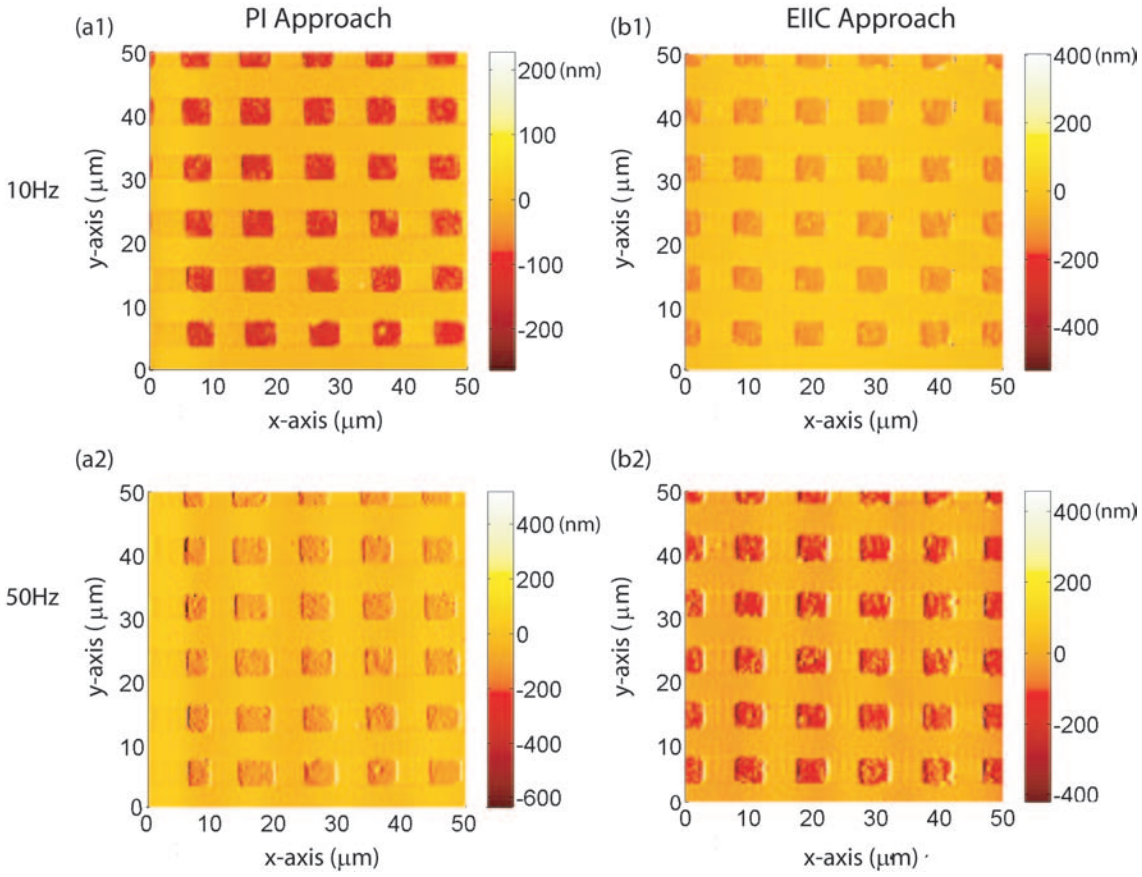

Figure 2.9 Comparison of the images obtained by using the PI controller (a1, a2) with those obtained by using EIIC approach (b1, b2) at the scan rates of 10 Hz (a1, b1) and 50 Hz (a2, b2).

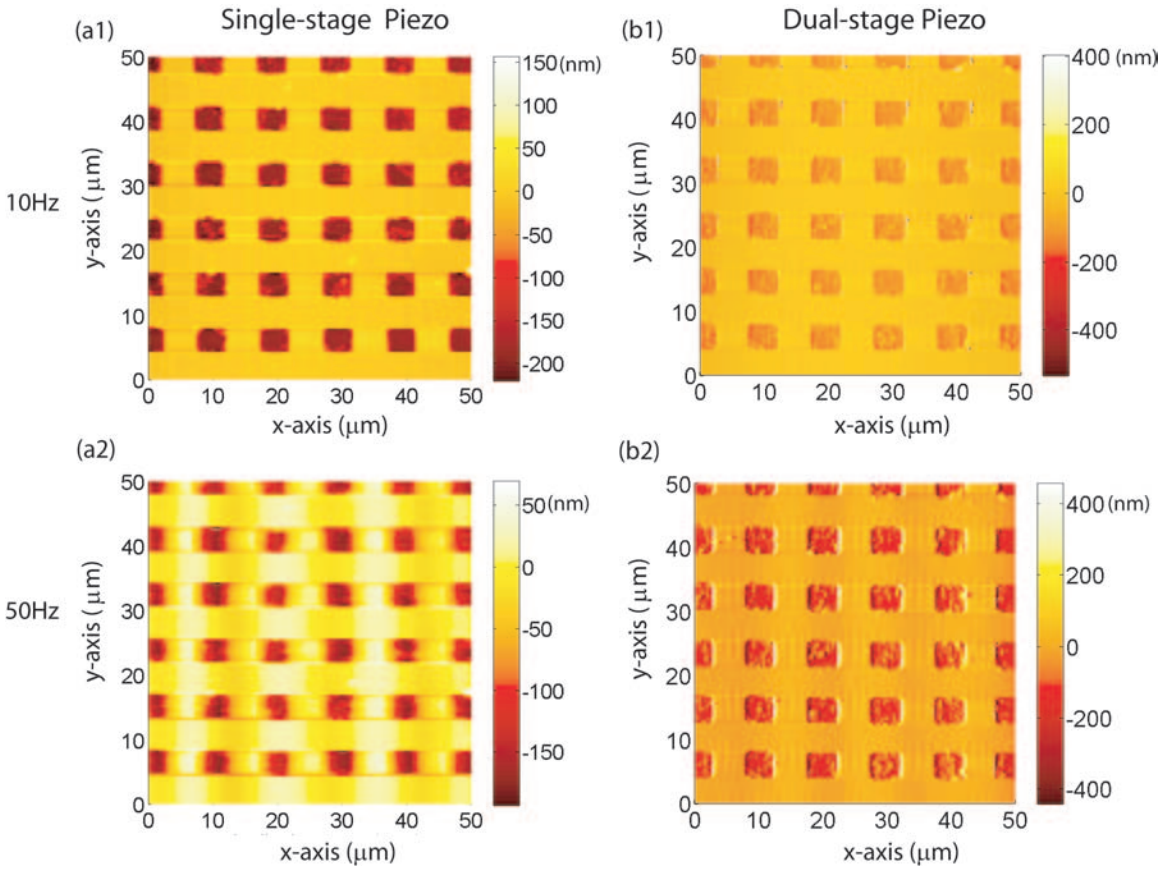

Figure 2.10 Comparison of the imaging results obtained by using the single-stage piezo actuator (a1, a2) with those obtained by using the dual-stage piezo actuator (b1, b2) at scan rate of 10 Hz (a1, b1) and 50 Hz (a2, b2). The EIIC technique was used for lateral scanning in all cases.

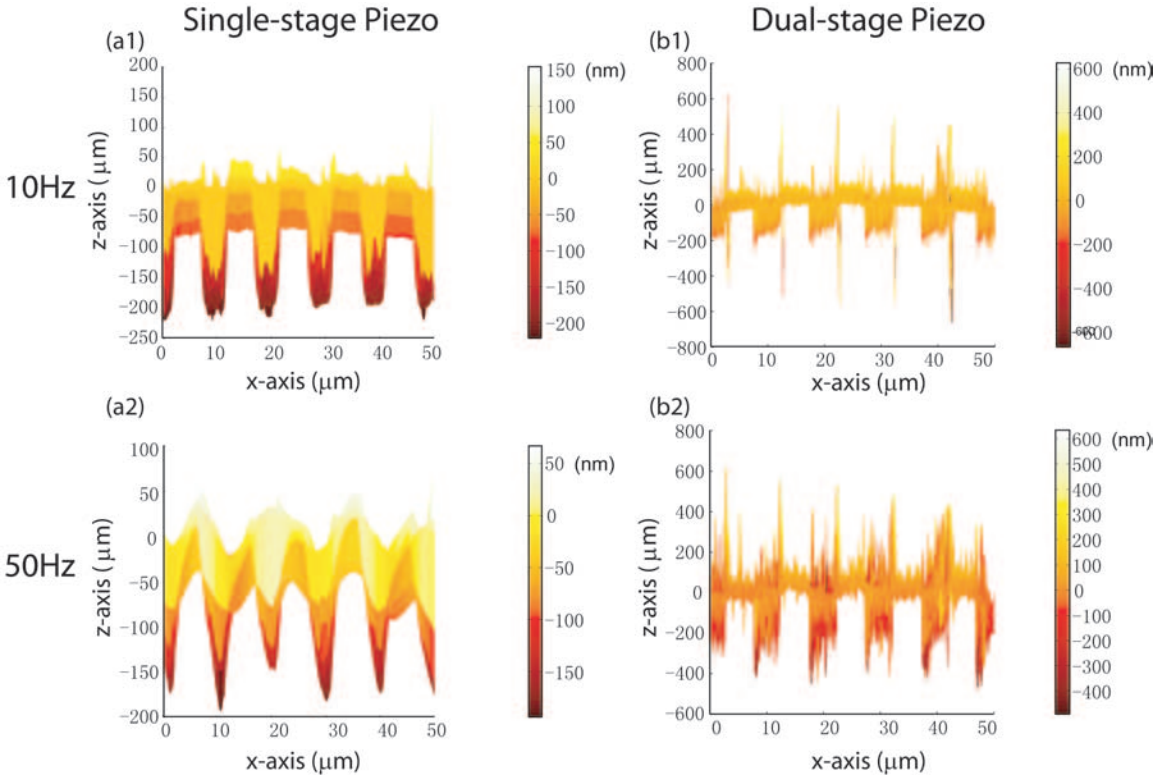

Figure 2.11 Comparison of the cross section images in $x-z$ direction by using the single-stage piezo actuator(a1, a2) with those by using the dual-stage piezo actuator (b1, b2) at the scan rate of 10 Hz (a1, b1) and 50 Hz (a2, b2).

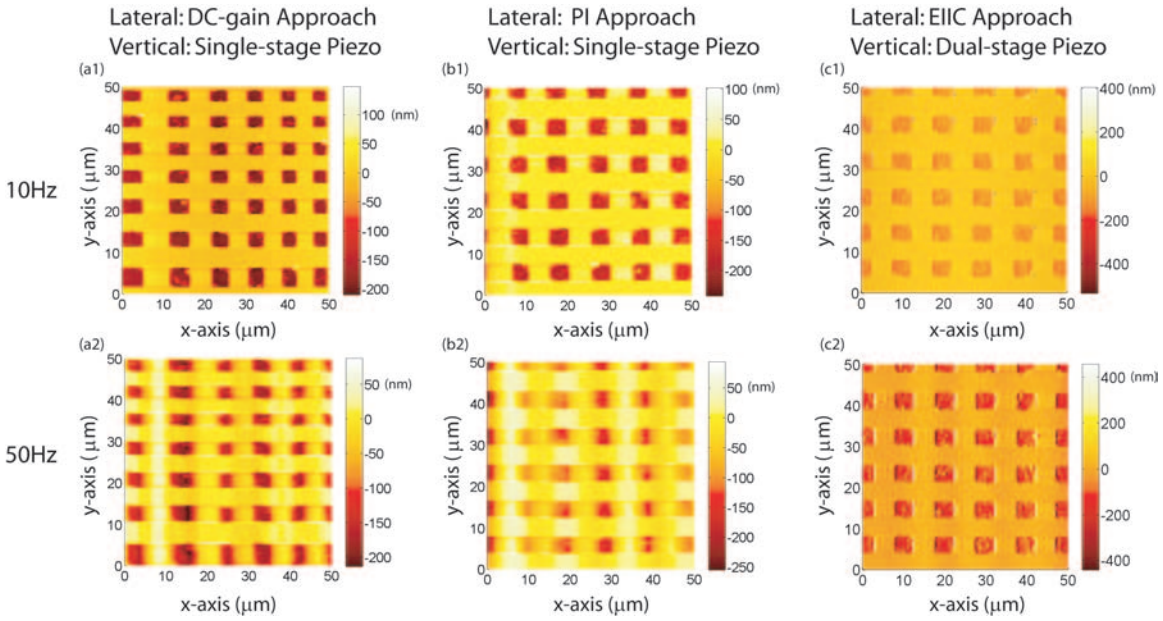

Figure 2.12 Comparison of the images obtained by using the DC-gain method along with single-stage actuator (a1, a2) and those obtained by using the PI controller along with single-stage actuator (b1, b2) with those obtained by using the proposed integrated approach (c1, c2) at the scan rates of 10 Hz (a1, b1, c1) and 50 Hz (a2, b2, c2).

CHAPTER 3. A CONTROL APPROACH TO HIGH-SPEED LARGE-RANGE PROBE-BASED NANOFABRICATION

3.1 INTRODUCTION

In this paper, an iterative feedforward control approach to achieve high speed and large range in probe-based nanofabrication is presented. Recently, probe-based nanofabrication using tools such as scanning probe microscope (SPM) has attracted many interests. Current probe-based nanofabrication processes (11)-(15), however, are limited by the low-throughput of the process, which, in turn, hurdles their practical implementations. Although such a low-throughput can be improved through hardware improvements such as parallel probes (15), the throughput is eventually limited if the fabrication is slow due to the hardware adverse effects (22). During high-speed, large-range fabrication, hardware adverse effects can lead to large positioning errors of the probe relative to the sample, and as a result, large defects in the nanopatterns/parts fabricated. The contribution of this article is the implementation of a recently-developed inversion-based iterative control approach (3) to compensate for the adverse hardware effects.

Precision positioning during high-speed, large-range motion is needed in probe-based nanofabrication. It has become evident that probe-based methods to fabricating nanoscale structures and devices are promising (because of their low cost and significant technical potential) (38). Various nanofabrication processes have been proposed (11)-(15; 39). All of these processes require the precision positioning of the probe relative to the sample, and thereby, are confronted by the same challenge—maintaining precision (probe-to-sample) positioning during high-speed, large-range operation. Large positioning errors can be generated during high-speed, large-range fabrication, which will not only lead to large defects in the fabricated structures or devices, but also result in damage of the probe (when the sample is hard) , the sample (when the sample is soft), or both. Moreover, unlike other probe-based applica-

tions (such as SPM imaging) where the motion in one axis is substantially slower than that in other axes, the motion control in probe-based nanofabrication can can be very demanding in all 3-D axes. As a result, positioning errors in different axes can be superimposed and lead to large distortions in the final structure/device fabricated. Additionally, when the fabrication speed is high and/or the operation range is large, the cross-axis dynamics coupling of piezo actuators (1) can become large, resulting in large fabrication distortions as well. Therefore, it is important to maintain the precision positioning of the probe relative to the sample in all *x*-*y*-*z* axes during high-speed, large-size nanofabrication.

Advanced control techniques can be used to improve positioning precision during high-speed, large-range motion. For example, it has been demonstrated recently that the output tracking in repetitive operations can be substantially improved by using the inversion-based iterative control (IIC) techniques (1; 22; 2). A main advantage of iterative control approach is the exploitation of the noncausality gained from the repetitive nature of the applications, particularly for nonminimum-phase systems such as piezo actuators in SPM (34). Also, it has been shown recently that the IIC approach can compensate for both hysteresis and dynamics effects of piezo actuators (22). The model-less iterative control (MIIC) employed in this article further extends the IIC approach (1), by eliminating the need for the dynamics modeling process in the control algorithm. Therefore, constraints related to the modeling process and the model accuracy are removed. The efficacy of the MIIC algorithm for precision positioning has been demonstrated through experiments (3; 40). Specifically, we note that in nanofabrication, the desired trajectory is usually specified a priori, and the environment tends to be well maintained. Therefore, it is advantageous to utilize iterative control techniques such as MIIC in probe-based nanofabrication.

The main contribution of the article is the use of the MIIC technique to probe-based nanofabrication using SPM. Particularly, the MIIC technique is utilized to compensate for the dynamics-coupling effect in multi-axis motions, as well as to account for the hysteresis and the dynamics effects in the motion of each individual *x*, *y* and *z* axis. The approach is illustrated by implementing it on SPM to mechanically scratch a challenging pattern (pentagram) on a gold-coated silicon sample surface. The experimental results show that even at a fabrication speed as high as 4.5 mm/sec, a large size pentagram pattern ($\sim$50

μm by $\sim$50 μm) can still be accurately fabricated by using the proposed approach. Furthermore, a dashed-line pentagram pattern was also fabricated, and the experimental results obtained demonstrate the efficacy of the proposed method for high-speed 3-D nanofabrication.

3.2 MIIC APPROACH TO PROBE-BASED NANOFRABRICATION

In this section, the use of MIIC technique (3) in probe-based nanofabrication is presented. We start with briefly describing the probe-based nanofabrication process.

3.2.1 Probe-Based Nanofabrication

In probe-based nanofabrication, a micro-machined probe is precisely positioned with respect to the sample surface during the motion on (or closely-above) the sample surface (see Fig. 3.1) to locally induce surface modification along the path, resulting in nanoscale features on the sample surface (such as lines or dots). Such a surface modification can be achieved, for example, through mechanical scratching followed by an etching process (12; 13), or, through thermal effect as exemplified in the IBM Millipede system (15). Alternatively, probe-based nanofabrication can also be achieved by introducing external effects such as electrical field (11), laser beam (39), and chemical compound (via probe coating) (14). In all these mechanisms, maintaining the probe-to-sample positioning precision is critical, because the probe-to-sample positioning error is directly translated to the defects in the fabricated nano-structures/devices. The probe-sample precision positioning becomes challenging when the nanofabrication is at high speed and large range, due to the excitation of adverse effects including the cross-axis dynamics coupling, the hysteresis, as well as the vibrational dynamics effects (22; 1; 23).

3.2.2 MIIC Approach to Multi-axis Motion Control

We propose to utilize the recently-developed MIIC approach (3) to compensate for the above adverse effects during probe-based nanofabrication. Iterative learning control (ILC) approach is attractive because in nanofabrication, the desired trajectories for all x-y-z axes are usually pre-specified and repetitive. Therefore, it is possible to utilize the entire trajectory tracking from the previous iteration

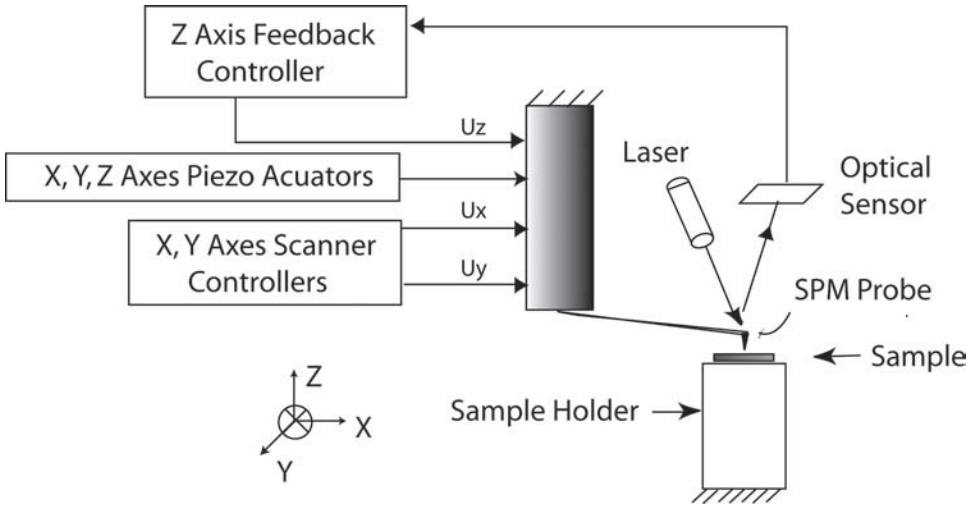

Figure 3.1 The schematic diagram of the SPM system.

to generate the control input at the current time instant. In other words, ILC approach provides the possibility to explore the noncausality in nanofabrication to enhance the precision positioning. Thus, it is advantageous to use the inversion-based iterative control technique to achieve high-speed nanofabrication.

The MIIC algorithm is described in frequency domain as

$$\begin{aligned} u_0(j\omega) &= \alpha y_d(j\omega) \\ u_{k+1}(j\omega) &= \frac{u_k(j\omega)}{y_k(j\omega)} y_d(j\omega), \\ &\quad (\text{for } u_k(j\omega) \neq 0,\ y_k(j\omega) \neq 0,\ k \geq 1) \end{aligned} \tag{3.1}$$

where $\alpha \neq 0$ is a pre-chosen constant (e.g., α can be chosen as the estimated DC-gain of the system dynamics), $f(j\omega)$ denotes the Fourier transform of the signal $f(t)$, $y_d(j\omega)$ is the desired output trajectory, and $u_k(j\omega)$ and $y_k(j\omega)$ are the input and the output obtained from the k^{th} iteration, respectively (see Fig. 3.2).

The MIIC technique extends the inversion-based iterative control (IIC) technique proposed in (1). The MIIC algorithm (Eq. (3.1)) can be transformed from the IIC algorithm by replacing the inverse of the dynamics model, $G_{ff}^{-1}(j\omega)$, in the IIC algorithm (see Eq. (9) in (1)) with $u_k(j\omega)/y_k(j\omega)$, and setting

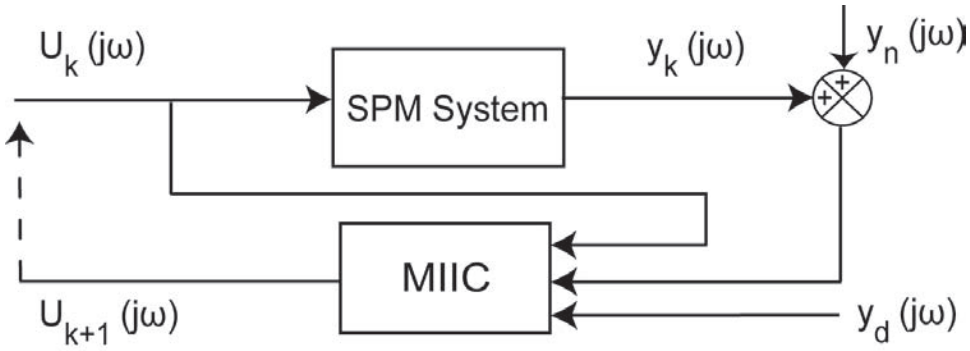

Figure 3.2 The block diagram of the MIIC algorithm.

the iterative coefficient $\rho(\omega) = 1$. Such a transformation implies that the dynamics modeling process is eliminated in the MIIC algorithm, whereas the IIC algorithms require a reasonably-good dynamics model of the system, and the convergence rate (i.e., the choice of the iterative coefficient) depends on the model accuracy. Thus, the MIIC technique alleviates these modeling-related constraints and thereby can achieve better tracking performance, particularly when the desired output trajectory is complex (41).

We note that in nanofabrication, the existing disturbance and measurement noise effects need to be addressed. The disturbance/noise effects can be modeled as an extra random output augmented to the system output—With that, the output becomes $\hat{y_k}(j\omega) = y_k(j\omega) + y_n(j\omega)$, where $y_k(j\omega)$ denotes the linear part of the system response, i.e., $y_k(j\omega) = G(j\omega)u_k(j\omega)$, and $y_n(j\omega)$ denotes the noise/disturbance. Then it can be shown that if the bound of the following noise/disturbance to the desired signal ratio (NSR), $\varepsilon(\omega)$, is less than $1-\sqrt{2}/2$, i.e., $\varepsilon(\omega) \triangleq |y_n(j\omega)|/|y_d(j\omega)| \leq [1-\sqrt{2}/2]$, the output tracking can be improved by using the MIIC algorithm (3),

$$\lim_{k\to\infty} \left| \frac{y_k(j\omega) - y_d(j\omega)}{y_d(j\omega)} \right| \leq \frac{2\varepsilon(\omega)[1-\varepsilon(\omega)]}{1-2\varepsilon(\omega)} < 1. \tag{3.2}$$

The above Eq. (3.2) shows that precision tracking of the desired trajectory over a broad frequency range can be achieved provided that the NSR $\varepsilon(\omega)$ is small (in that frequency range). The "trackable" frequency range can be larger than the open-loop bandwidth of the system (3; 40).

3.2.3 Compensating for the Cross-Axis Coupling Effect Using MIIC

Compensating for cross-axis dynamics coupling existing in multi-axis motion control (1; 42; 43). is particularly important when fabricating 3-D nano-devices/patterns, because the motions in all x-y-z axes can be complicated and at high speed. Although the cross-axis coupling effects can be accounted for by considering the 3-D (x-y-z axes) SPM dynamics as a multi-input-multi-output (MIMO) system, and then designing a MIMO controller accordingly (44), such an approach involves complicated online computations, and its performance can be hampered by the possibly large model uncertainties. In this article, MIIC algorithm (Eq. (3.1)) is used to compensate for, not only the dynamics and hysteresis effects in each axis (3), but also the cross-axis dynamics coupling effects. Such a cross-axis coupling is pronounced from the large-range lateral x-y axes motion to the vertical z-axis motion, and becomes more significant in high-speed operation. As schematically shown in Fig. 3.3, the x-y-to-z coupling-caused displacement $y_{zxy}(j\omega)$ is augmented to the displacement of z-axis itself $y_{zz}(j\omega)$, leading to the total z-axis displacement $y_z(j\omega)$ as,

$$\begin{aligned} y_z(j\omega) &= G_{zz}(j\omega)u_z(j\omega) + G_{zx}(j\omega)u_x(j\omega) \\ &\quad + G_{zy}u_y(j\omega) \\ &\triangleq y_{zz}(j\omega) + y_{zxy}(j\omega). \\ &(y_{zxy}(j\omega) \triangleq G_{zx}(j\omega)u_x(j\omega) + G_{zy}(j\omega)u_y(j\omega)) \end{aligned} \tag{3.3}$$

Thus first, the x-y-to-z coupling-caused displacement $y_{zxy}(j\omega)$ is measured by applying the control input to the lateral x-y axes on a hard flat reference sample (e.g., a silicon sample or a sapphire calibration sample). Then, the desired z-axis displacement $y_{z,d}(j\omega)$ is modified by subtracting with the measured coupling-caused displacement $y_{zxy}(j\omega)$,

$$\hat{y}_{z,d}(j\omega) = y_{z,d}(j\omega) - y_{zxy}(j\omega), \tag{3.4}$$

and the MIIC technique is applied to the z-axis only (with no lateral displacement, i.e., $y_{zxy}(j\omega) = 0$ in (3.4)) to find the control input $u_z^*(j\omega)$ that tracks the modified z-axis desired trajectory, i.e.,

$$G_{zz}(j\omega)u_z^*(j\omega) = y_{zz}(j\omega) \longrightarrow \hat{y}_{z,d}(j\omega) \tag{3.5}$$

Finally, the control inputs for both the lateral x-y and z-axis tracking are applied simultaneously. As a result, the x-y-to-z coupling is removed and precision positioning in all x-y-z axes is achieved. We

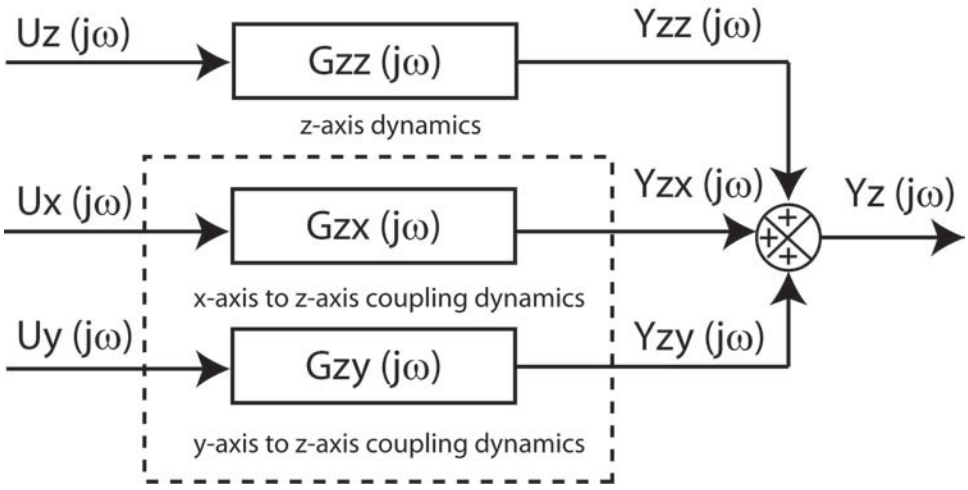

Figure 3.3 The z-axis AFM dynamics with x-y-to-z coupling effect.

note that similar approach to compensate for the cross-axis coupling has been proposed in (1). The above method extends the work in (1) for nanofabrication by achieving precision trajectory tracking in all three x-y-z axes at the same time.

3.3 EXPERIMENTAL EXAMPLE

We illustrate the MIIC approach to probe-based nanofabrication through experiments. It is demonstrated that by using the MIIC approach, high-speed nanofabrication of a challenging pattern (pentagram) of large size can be achieved. We start with briefly describing the nanofabrication process based on mechanical scratching.

3.3.1 Nanofabrication Based on Mechanical Scratching

The experiments were carried out under ambient condition on a SPM system (Dimension 3100, Veeco Instruments Inc.) with a rectangular-shape cantilever coated with wear-resistant material. The nominal stiffness of the probe is 40 N/m (stiffer probes like the stainless steel cantilever with diamond tip can be used to further reduce weariness and increase the smoothness of the fabricated pattern). By applying a relatively large loading force to the SPM probe on the sample surface, and dragging the probe to track the desired geometry path, patterns of nanoscale feature can be fabricated. The fab-

ricated pattern can be examined by imaging the sample surface using the same SPM system with a substantially lower loading force. In applications, the mechanical-scratching method is usually used to fabricate fine patterns on a soft metal or polymer material such as PMMA (45). For harder material such as silicon, the mechanical-scratching technique has been successfully used to fabricate multilayer nanometer devices along with an etching process (46). We note that as discussed before, the precision positioning problem ubiquitously exists in probe-based nanofabrication processes. Therefore, we expect that the proposed MIIC technique can be equally applied to other probe-based nanofabrication processes as well.

3.3.2 Experimental setup

The SPM system utilized in this article uses piezotube actuators to position the SPM probe with respect to the sample in all *x*-*y*-*z* axes. All the control inputs were generated by using MATLAB-xPC-target (Mathworks, Inc.), and sent through a data acquisition card to drive the high-voltage amplifiers for the corresponding piezotube actuators.

In the following experiments, two types of pentagram (one with continuous lines, and the other with dashed lines) were chosen as the desired patterns to be fabricated. When fabricating the continuous-line pentagram pattern, contact mode SPM was used to maintain the cantilever deflection around a setpoint value (i.e., to maintain a constant tip-sample interaction force) by using the feedback controller of the SPM system for the *z*-axis probe positioning. When fabricating the dashed-line pentagram pattern, the *z*-axis feedback control was turned off, and the vertical position of the *z*-axis piezo actuator was controlled by applying the feedforward input obtained from the MIIC technique to track the desired *z*-axis trajectory. The fabrication of the dashed-line pentagram pattern required the up-and-down vertical motion of the probe. Thus, such an experiment evaluated the MIIC algorithm for fabricating 3-D structures. The desired pentagram pattern (size: $\sim$50 μm by $\sim$50 μm) and the corresponding desired trajectories for each *z*, *x*, and *y* axis are shown in Fig. 3.4 (a), (b), (c), and (d), respectively. Particularly, an isosceles trapezoidal wave was chosen as the desired *z*-axis waveform. The use of the isosceles trapezoidal wave rather than square wave was to reduce the oscillations after the up-down transitions.

The entire pentagram pattern composed a total of 20 dash lines evenly spaced (Fig. 3.4 (b)).

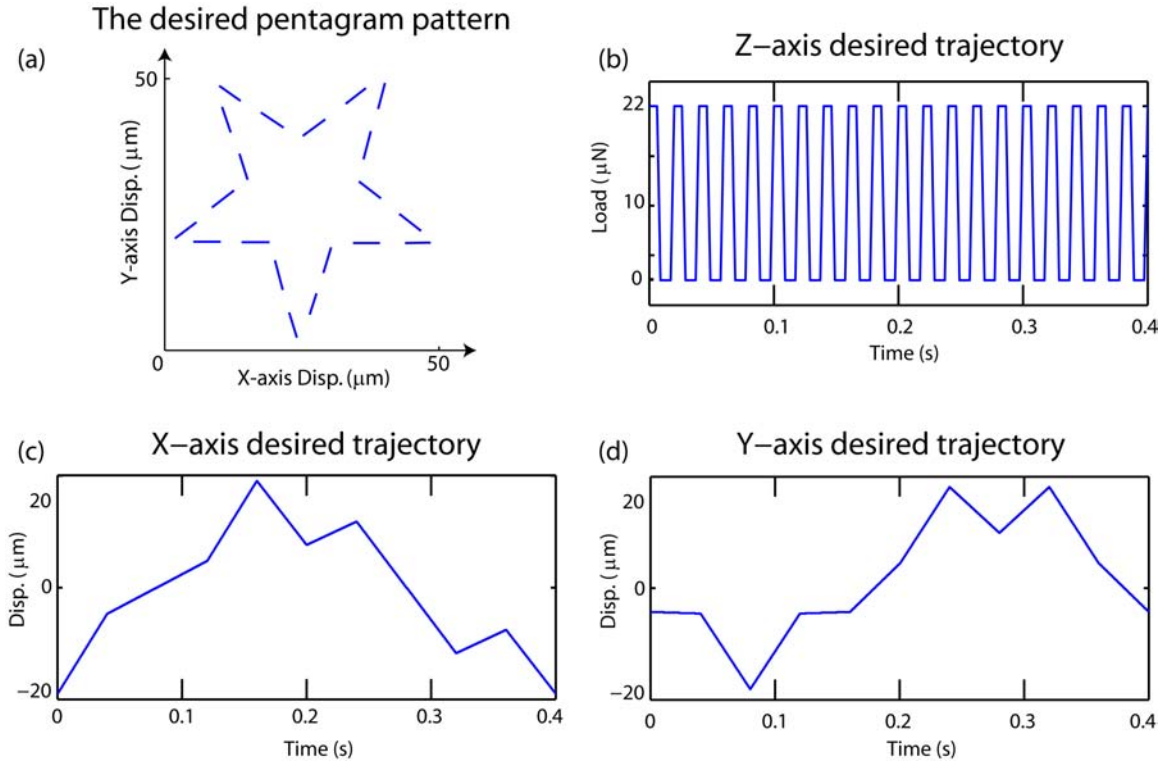

Figure 3.4 The desired trajectories of the dash-line pentagram pattern: (a) the entire trajectory, (b) the z-axis trajectory, (c) the x-axis trajectory, and (d) the y-axis trajectory.

3.3.3 SPM dynamics

The SPM dynamics in each axis (x, y, and z) was measured experimentally. For example, the lateral x-axis dynamics from the input voltage to the displacement output of the piezotube actuator was measured using a dynamic signal analyzer (DSA, Hewlett Packard 356653A). Also, the dynamics uncertainty was experimentally quantified by measuring the frequency responses under different driven input levels (20 mv, 40 mv, and 60 mv), as shown in Fig. 3.5 for the frequency range $\omega \in [0,3]$ kHz. When measuring the z-axis SPM dynamics (from the input voltage of the z-axis piezo actuator to the cantilever deflection), the cantilever probe was pressed onto a hard silicon sample with a preload constant force and a sinusoidal oscillatory force of small amplitude was applied with the sinusoidal

frequency sweeping over the measured range (i.e., the swept-sine method). Therefore, the obtained frequency response should mainly contain the dynamics of the piezoelectric actuator and the cantilever along with the mechanical fixture connecting them (as the surface is hard). The measured frequency response is shown in Fig. 3.6 for the frequency range $\omega \in [0,4]$ kHz. We note that the implementation of the MIIC algorithm did not require an a priori dynamics modeling process (see Eq. 3.1). Instead, the SPM dynamics in Fig. 3.5 and Fig. 3.6 were measured to evaluate the performance of the proposed MIIC technique for high-speed nanofabrication.

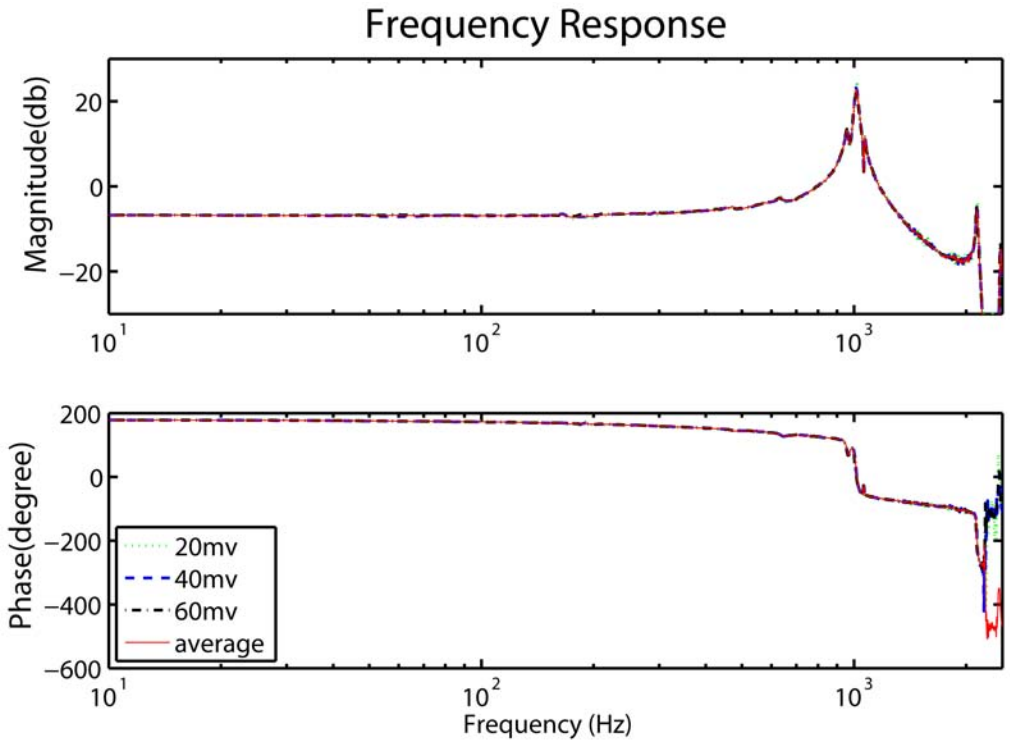

Figure 3.5 The frequency responses of the x-axis piezoelectric actuator on the SPM, measured with three different input amplitude levels (20 mv, 40 mv, and 60 mv), with comparison to the averaged response.

3.3.4 Tracking Results and Discussion

In the experiments, the MIIC technique was applied to achieve precision tracking in all x-y-z axes simultaneously (as described in Sec. 3.2), and then, the converged inputs were used to fabricate the

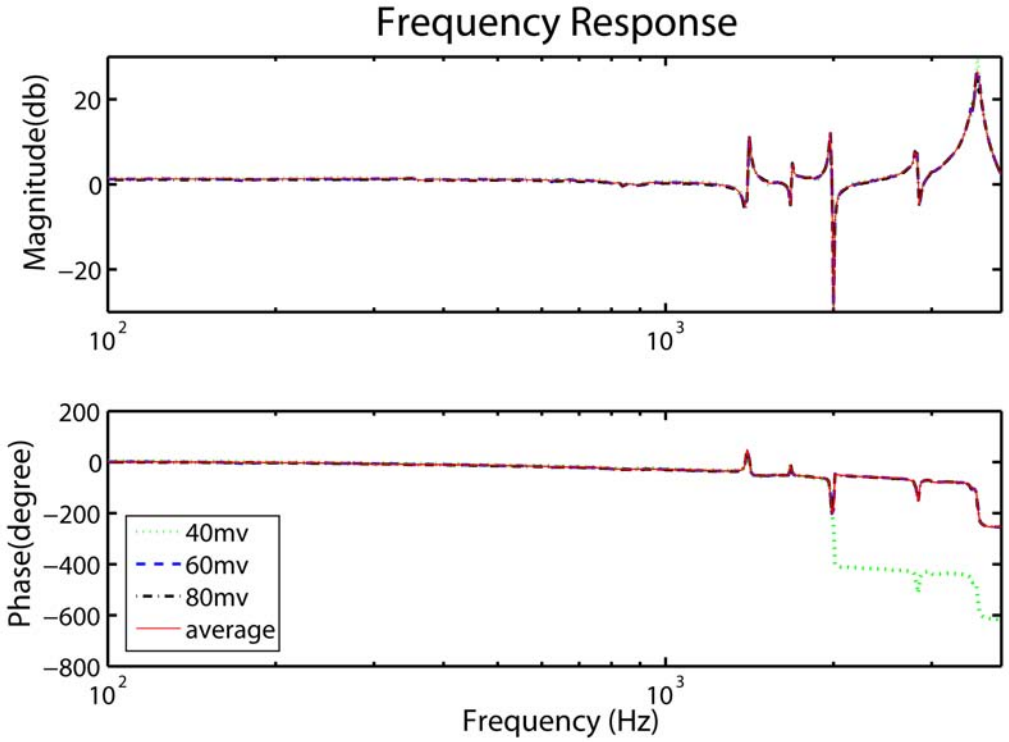

Figure 3.6 The frequency responses of the z-axis piezoelectric actuator on the SPM, measured with three different input amplitude levels (40 mv, 60 mv, and 80 mv), with comparison to the averaged response.

pattern by applying a large load force ($\sim$22 μN) to the cantilever. For comparison, we also used the DC-gain method to fabricate the pentagram pattern, where the control input was generated by scaling the desired output with the DC-gain of the piezo actuator. The DC-gain method does not account for the hysteresis nor the vibrational dynamics effects, thereby the fabricated patterns demonstrated these adverse effects on the fabrication quality.

To compensate for the x-y-to-z coupling effect, the coupling-caused z-axis displacement was measured from the cantilever deflection (in vertical direction) when pressing the probe onto a hard silicon sample of nanoscale flatness (the surface roughness was within a couple of nanometers) and applying the x-axis and y-axis control inputs for tracking the x, y-axis desired trajectories, respectively (see Fig. 3.4 (c), (d)). Then the modified z-axis desired trajectory was obtained as described in Sec. 3.2.3, and the MIIC

algorithm was used to obtain the control input to track this modified z-axis desired trajectory. Finally, this control input was applied to the z-axis when the control inputs to the other two axes were applied, simultaneously. We note that for this SPM system, other cross-axis coupling effects including vertical to lateral and between lateral x-y axes were small and negligible.

The experimental tracking results in all x-y-z axes were acquired and compared. Three different fabrication rates (5 Hz, 15 Hz and 25 Hz) were tested in the experiment, where the fabrication rate was defined as the rate to finish the fabrication of the entire pattern once. The corresponding average lateral speed for the three fabrication rates were at $\sim$0.9 mm/sec, $\sim$2.7 mm/sec, and $\sim$4.5 mm/sec, respectively. At these three fabrication rates, the corresponding z-axis waveform frequency (for fabricating the dashed-line pentagram pattern) was at 100, 300, and 500 Hz, respectively. In Fig. 3.7, the lateral x-axis tracking results for the fabrication rates of 5 Hz and 25 Hz obtained by using the converged MIIC inputs are compared with the desired trajectory as well as those obtained by using the DC-gain method. To evaluate the z-axis tracking (with no lateral x-y axes displacement), the modified desired trajectory was used (to account for the x-y-to-z coupling) when the MIIC was applied, and the original desired trajectory was used when the DC-gain method was applied. The tracking results for the waveform frequencies of 100 Hz and 500 Hz (corresponding to the fabrication rates of 5 Hz and 25 Hz, respectively) are shown in Fig. 3.8 for the MIIC method and Fig. 3.9 for the DC-gain method. During the implementation of the MIIC technique, the iterations were stopped when the tracking error cannot be further reduced. Finally, the z-axis tracking during the fabrication process (i.e., when all x-y-z axes inputs were applied simultaneously) was also compared for the MIIC method and the DC-gain method with respect to the original z-axis desired trajectory, as shown in Fig. 3.10.

The tracking performance was also evaluated by quantifying the relative RMS tracking error and the relative maximum tracking error, as listed in Table. 3.1 for the lateral tracking and Table. 3.2 for the vertical tracking, where the relative maximum tracking error $E_M(\%)$, and the relative RMS tracking error $E_{RMS}(\%)$ are defined as

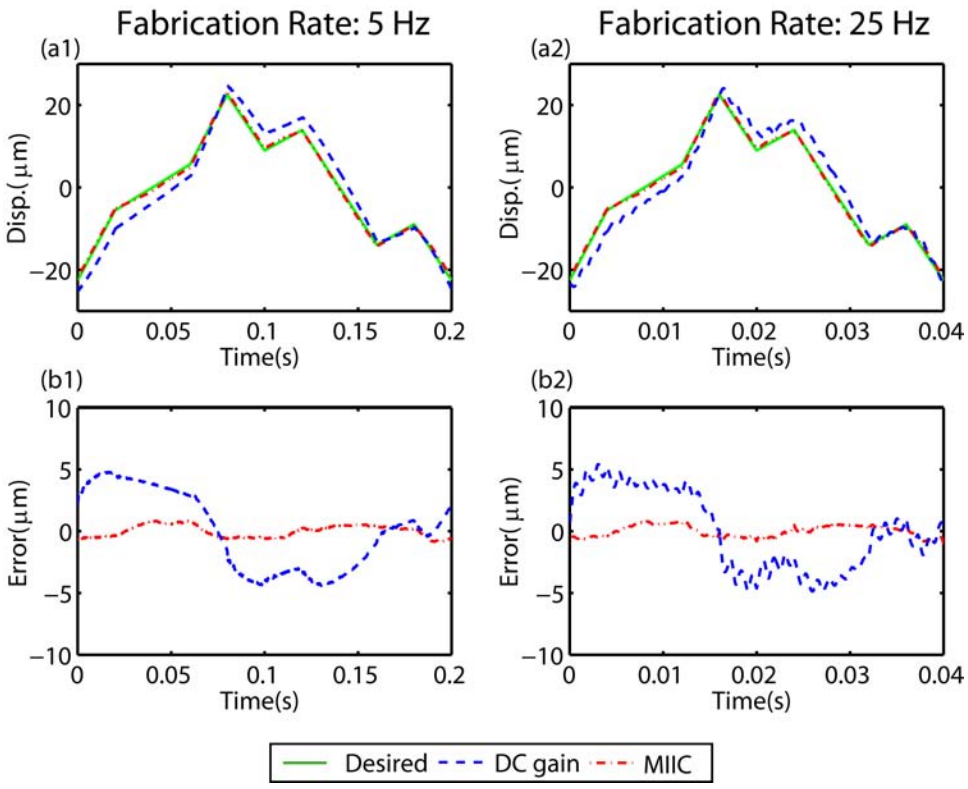

Figure 3.7 Comparison of the lateral x tracking results obtained by using the MIIC technique with those by using the DC-gain method at 5 Hz (a1), 25 Hz (a2), and comparison of the corresponding tracking errors at 5 Hz (b1), 25 Hz (b2), respectively.

$$E_M(\%) \triangleq \frac{\|y_d(\cdot) - y_k(\cdot)\|_\infty}{\|y_d(\cdot)\|_\infty} \times 100\%,$$
$$E_{RMS}(\%) \triangleq \frac{\|y_d(\cdot) - y_k(\cdot)\|_2}{\|y_d(\cdot)\|_2} \times 100\%. \tag{3.6}$$

Discussion The experimental results demonstrate that precision positioning in lateral x-y axes motion can be achieved by using the MIIC algorithm during large-range, high-speed nanofabrication. As the lateral displacement range was large (50 μm), the hysteresis effect was pronounced, and large positioning errors were generated. As shown in Fig. 3.7 (a1) and (b1), with the DC-gain method, the hysteresis-caused relative maximum error $E_M(\%)$ was over 10% of the total displacement range when the fabrication rate was slow (5 Hz). Such a large positioning error was substantially reduced by us-

Table 3.1 Comparison of the tracking errors in X-axis obtained by using the DC–gain method and the MIIC approach at different fabrication rates.

Error	$E_M(\%)$			$E_{RMS}(\%)$		
Fab. Rate	**5 Hz**	**15 Hz**	**25 Hz**	**5 Hz**	**15 Hz**	**25 Hz**
Speed (mm/s)	**0.64**	**1.93**	**3.21**	**0.64**	**1.93**	**3.21**
1^{st} Iter.	3.81	3.67	4.23	1.49	1.39	1.41
2^{nd} Iter.	2.04	2.12	2.11	1.15	1.12	1.20
3^{rd} Iter.	1.80	1.90	2.44	1.09	1.05	1.13
4^{th} Iter.	1.88	1.97	2.30	0.99	1.09	1.14
DC-gain	10.66	11.53	12.05	7.02	6.92	7.16

Table 3.2 Comparison of the tracking errors in Z-axis obtained by using the DC–gain method, and the MIIC approach at different fabrication rates.

Error	$E_M(\%)$			$E_{RMS}(\%)$		
Fab. Rate	**5 Hz**	**15 Hz**	**25 Hz**	**5 Hz**	**15 Hz**	**25 Hz**
1^{st} Iter.	5.18	5.84	7.57	0.78	0.86	1.80
2^{nd} Iter.	2.03	2.30	3.28	0.55	0.64	0.87
3^{rd} Iter.	1.14	1.20	2.06	0.34	0.44	0.50
4^{th} Iter.	1.16	1.18	2.21	0.34	0.43	0.57
DC-gain	26.15	52.81	74.82	9.07	18.48	28.31

ing the MIIC algorithm— the relative RMS error $E_{RMS}(\%)$ and the relative maximum error $E_M(\%)$ were reduced to 0.99% and 1.88%, respectively. As the fabrication rate was increased to 25 Hz, the vibrational dynamics effect was augmented to the hysteresis effect, resulting in even larger tracking errors. However, precision tracking was still maintained when using the MIIC approach— $E_{RMS}(\%)$ and $E_M(\%)$ were only 1.14% and 2.30%, respectively (see Fig. 3.7 (a2), (b2) and Table 3.1). We note that for nanofabrication application, precision tracking in x and y axes are equally crucial, because even if the tracking error in each individual axis is small, a relatively large distortion can still be generated in the final fabricated pattern. Such an "amplification" of the positioning error is caused by the superposition of the errors in different axes. In the experiment, precision tracking in y axis was also achieved by using the MIIC technique. The simultaneous precision tracking in both x and y axes leaded to the precision fabrication of the continuous-line pentagram pattern.

When fabricating the dashed-line pentagram pattern, the frequency of the isosceles trapezoidal wave was much higher (20 times higher) than that in the lateral x-y axes. As a result, large probe oscillations in the vertical z-axis not only increased the roughness of the sample surface, but can also further damaged the probe, the sample, or both. By using the MIIC algorithm, however, even at the fabrication rate of 25 Hz, precision vertical z-axis tracking was still achieved—the $E_{RMS}(\%)$ was only 2% of that by using the DC-gain method (see Fig. 3.8, Fig. 3.9 and Table 3.2). Thus, the MIIC algorithm can effectively account for adverse effects during high-speed, large-size nanofabrication in both lateral and vertical directions.

The experimental results also showed that coupling-caused disturbance in multi-axis motion can also be effectively removed by using the proposed method (see Sec. 3.2.3). Comparing the modified z-axis desired trajectory (in Fig. 3.8) with the original one (in Fig. 3.9), we can see that the x-y-to-z coupling effect was substantial. The coupling-caused z-axis displacement was $\sim$40% of the (original) desired trajectory when the lateral x-y axes displacement was large (50 μm) and the velocity was at high speed (4.5 mm/sec). Such a large coupling-caused disturbance was augmented to the vibrational dynamics effect when all 3-D inputs were applied simultaneously during the nanofabrication of the dashed-line pentagram, resulting in much larger tracking error (than that if there were no coupling effect). This is evident by comparing with the DC-gain tracking result in Fig. 3.9. On the contrary, such a large coupling-caused disturbance was removed with the use of the proposed MIIC technique, and precision tracking of the original z-axis desired trajectory was achieved during the 3-D nanofabrication. Note that in Fig. 3.10, the small oscillations at the top and the bottom of the isosceles waves were generated because the SPM cantilever needed to be pulled out and pushed onto the sample surface during the fabrication. Therefore, the experimental results demonstrate that the proposed approach can achieve high-speed precision positioning in 3-D probe-based nanofabrication at large-size.

3.3.5 Nanofabrication Results and Discussion

Nanofabrication of continuous-line pentagram pattern Next, to fabricate the continuous-line pentagram pattern, the MIIC inputs were applied to the x and y axes simultaneously with a larger load force. Then the fabricated sample area was imaged immediately afterwards on the same SPM system. The SPM images of the fabricated patterns obtained by using the MIIC technique are compared with those obtained by using the DC-gain method in Fig. 3.11 for the three fabrication rates (5 Hz, 15 Hz and 25 Hz). For comparison, the desired pentagram pattern was also marked by the blue-dashed line in Fig. 3.11. As shown in Fig. 3.11, the MIIC technique effectively removed the fabrication distortion caused by the hysteresis and the vibrational dynamics effects. When the fabrication speed was relatively slow at 5 Hz (the corresponding averaged line speed was $\sim$0.9 mm/sec, see Fig. 3.11 (a1)), the distortion in the fabricated pattern was already obvious. Such pronounced distortions were mainly caused by the nonlinear hysteresis effect existing in both x- and y- axes piezo actuators (because the fabrication size was large, 50 μm). Particularly, the positioning errors were amplified due to the superimposition of the x-axis errors with the y-axis ones, caused mainly by the phase-delay and asynchronization between the x and the y axes. In contrast, the use of the MIIC approach effectively removed such fabrication distortions (see Fig. 3.11 (b1)). When the fabrication rate was increased to 15 Hz (the corresponding average line speed was $\sim$2.7 mm/sec), the tracking error caused by the vibrational dynamics became significant, resulting in large oscillatory distortions in the fabricated pattern when the DC-gain method was used (see Fig. 3.11 (a2)), which became even larger when the fabrication rate was further increased to 25 Hz (the average line speed was at 4.5 mm/sec, see Fig. 3.11 (a3)). Using the MIIC technique, precision tracking was still maintained during this high-speed, large-range fabrication. As shown in Fig. 3.11 (b2), (b3), the pattern distortion was very small, and the fabricated pattern almost overlapped with the desired one (marked by the blue-dashed line in Fig. 3.11). Therefore, the experimental results demonstrate that by using the MIIC approach, high-speed probe-based nanofabrication of 2-D pattern can be achieved.

Nanofabrication of the dashed-line pentagram pattern Next, the converged MIIC inputs for all the x-y-z axes were applied to the x, y, and z axes respectively at the same time (the z-axis feedback control

was turned off), and the dashed-line pentagram pattern was fabricated. Then the fabricated sample area was imaged immediately afterwards on the same SPM. The SPM images of the fabricated patterns obtained by using the MIIC technique are compared with those obtained by using the DC-gain method (applied to all 3-D axes) in Fig. 3.12 for the three fabrication rates (5 Hz, 15 Hz and 25 Hz). To avoid confusion, the desired pentagram pattern was not marked out in Fig. 3.12. We also examined the indentation depth of the dashed-line by the cross-section plot shown in Fig. 3.13—the indentation depth was $\sim$10 nm.

The experimental results demonstrated the efficacy of the proposed approach in achieving 3-D precision positioning during high-speed probe-based nanofabrication. When the fabrication rate was at 5 Hz, the distortions caused by nonlinear hysteresis and vibrational dynamics effects were already pronounced. As shown in Fig. 3.12 (a1), the dashed-lines in the pattern obtained by using the DC-gain method were curved (rather than straight) and varied in length. However, such large fabrication errors in the dashed lines were significantly reduced by using the MIIC method: the dash lines were straight and uniform in length, close to the desired ones (see Fig. 3.12 (b1) and Fig. 3.4 (a)). When the rate was increased to 15 Hz and 25 Hz, the hysteresis and dynamics caused pattern distortions became much more severe. As shown in Fig. 3.12 (a2, a3), the dashed lines were more curved and largely varied in length. On the contrary, such large pattern distortions were substantially reduced by using the proposed method. As a result, the pentagram patterns were close to the desired one (see Fig. 3.12 (b2), (b3)). To the best knowledge of the authors, Fig. 3.11 (b3) and Fig. 3.12 (b3) represent one of the fastest probe-based nanofabrication results ever achieved (in terms of the line speeds in both the lateral and the vertical directions). Therefore, the experimental results demonstrated that the MIIC approach can be effectively utilized for high-speed nanofabrication of large-size 3-D patterns.

3.4 CONCLUSION

A control approach to achieve probe-based high-speed nanofabrication at large range has been proposed. It was shown that the implementation of the MIIC technique to the SPM probe-based nanofabrication can effectively compensate for the nonlinear hysteresis and vibrational dynamics effects as well

as the dynamic coupling effect of piezotube actuator, thereby improve the fabrication throughput. The approach has been illustrated by implementing it to fabricate a pentagram via mechanical-scratching on a gold-coated silicon sample surface. The experimental results showed that the pentagram patterns of a size of $\sim$50 μm with both continuous and dashed-lines can be accurately fabricated at a high (averaged) line speed of 4.5 mm/sec. Therefore, the experimental results demonstrated that by using the proposed approach, precision position control can be achieved in the high-speed large-range multi-axes nanofabrication.

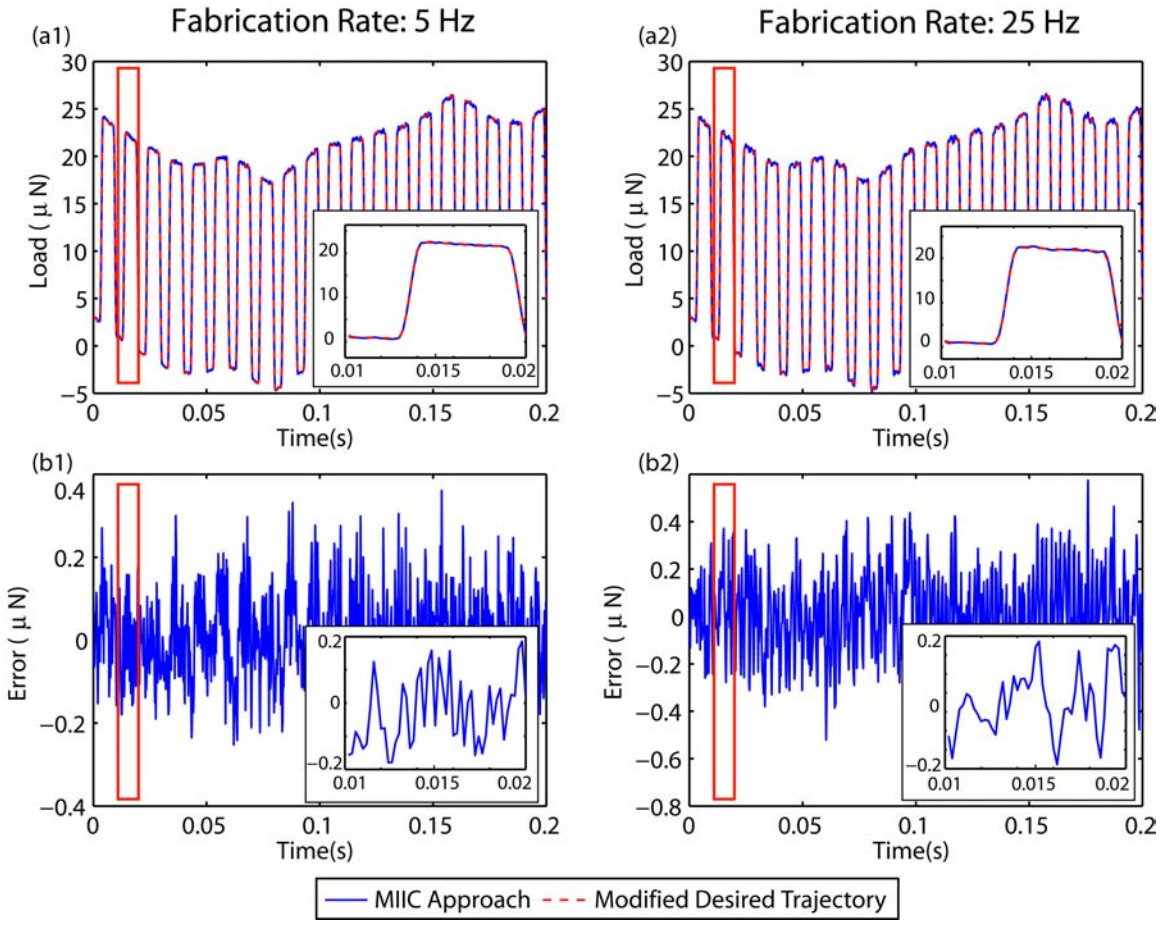

Figure 3.8 Comparison of the vertical z tracking results by using the MIIC technique with the modified desired trajectory at 5 Hz (a1), 25 Hz (a2), and comparison of the corresponding tracking errors at 5 Hz (b1), 25 Hz (b2), respectively, where the inserts are the zoomed-in view of the tracking (a1, a2) and the tracking error (b1, b2) within the dashed-rectangular window.

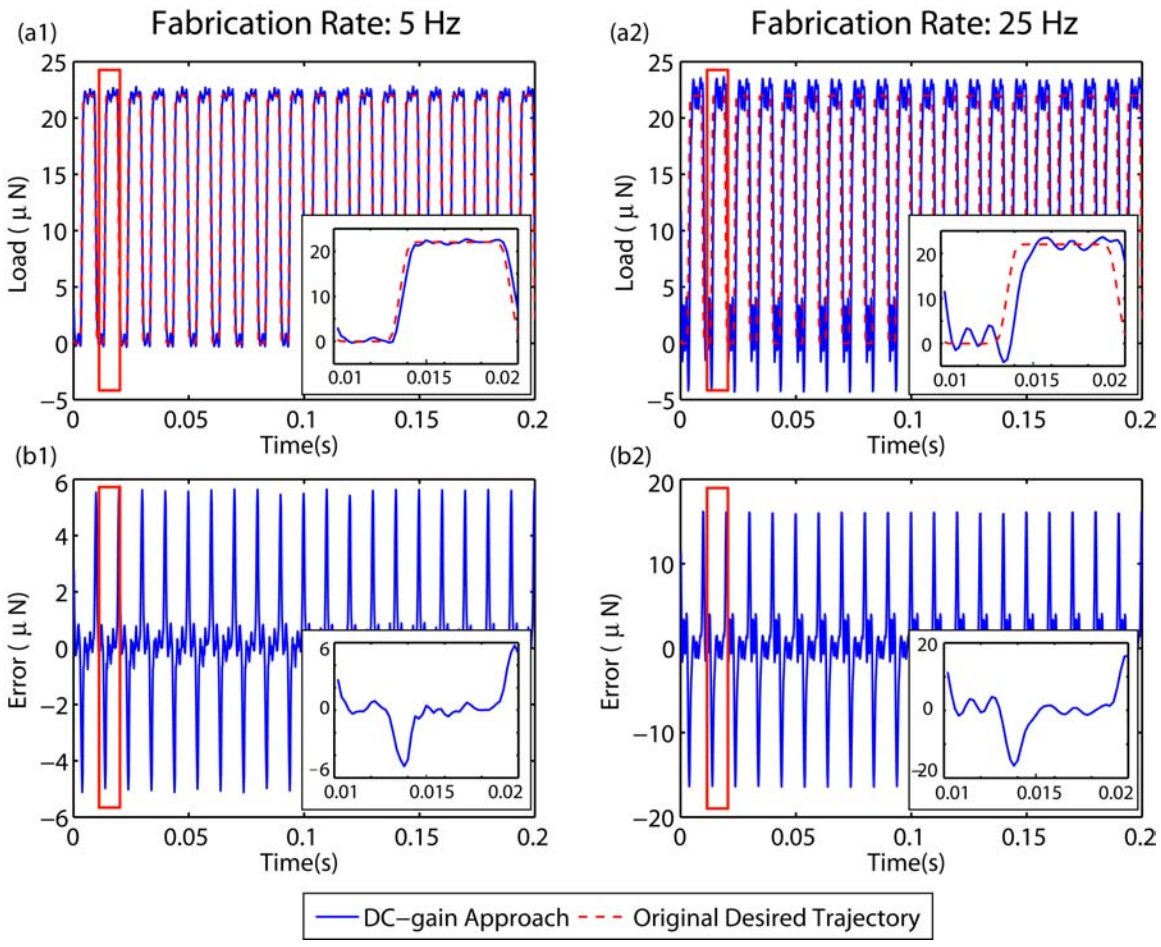

Figure 3.9 Comparison of the vertical z tracking results by using the DC-gain method with the original desired trajectory at 5 Hz (a1), 25 Hz (a2), and comparison of the corresponding tracking errors at 5 Hz (b1), 25 Hz (b2), respectively, where the inserts are the zoomed-in view of the tracking (a1, a2) and the tracking error (b1, b2) within the dashed-rectangular window.

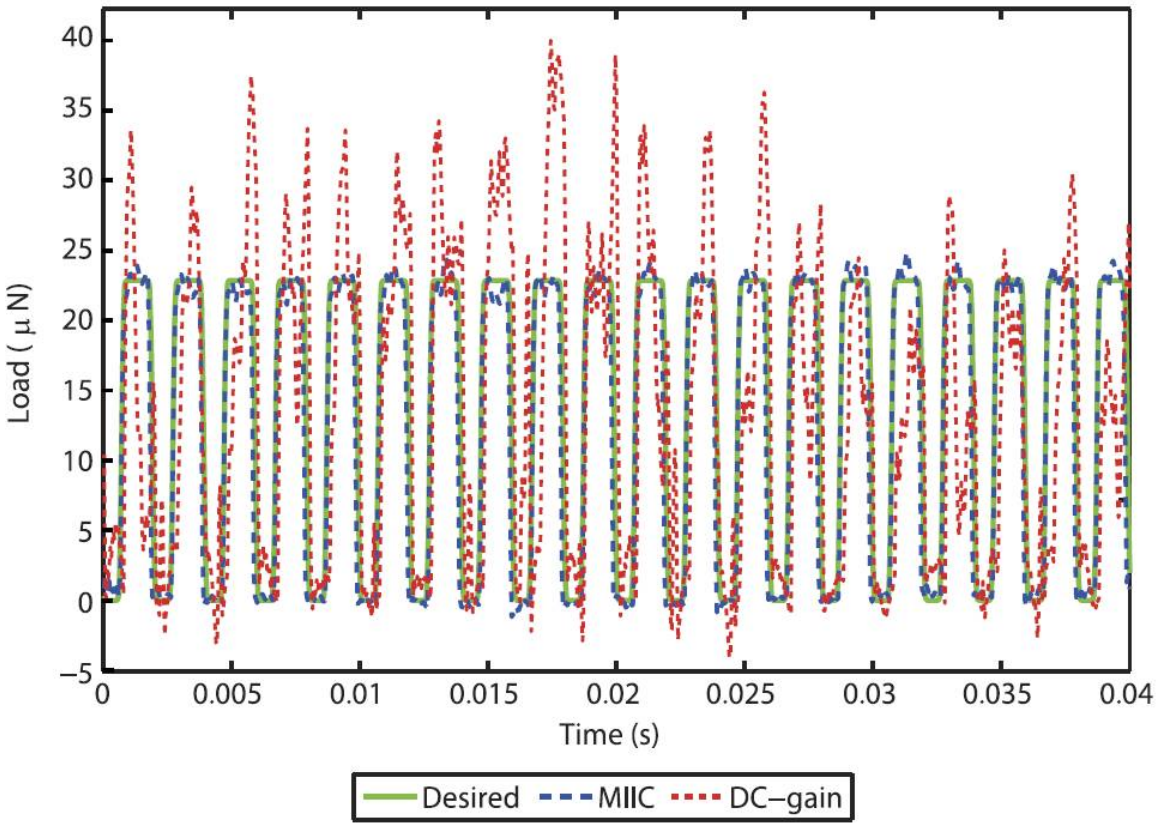

Figure 3.10 Comparison of the z-axis deflection signal by using the MIIC technique with that by using the DC-gain method at 25 Hz during the fabrication process (i.e., when the lateral x-y axes inputs were also applied simultaneously).

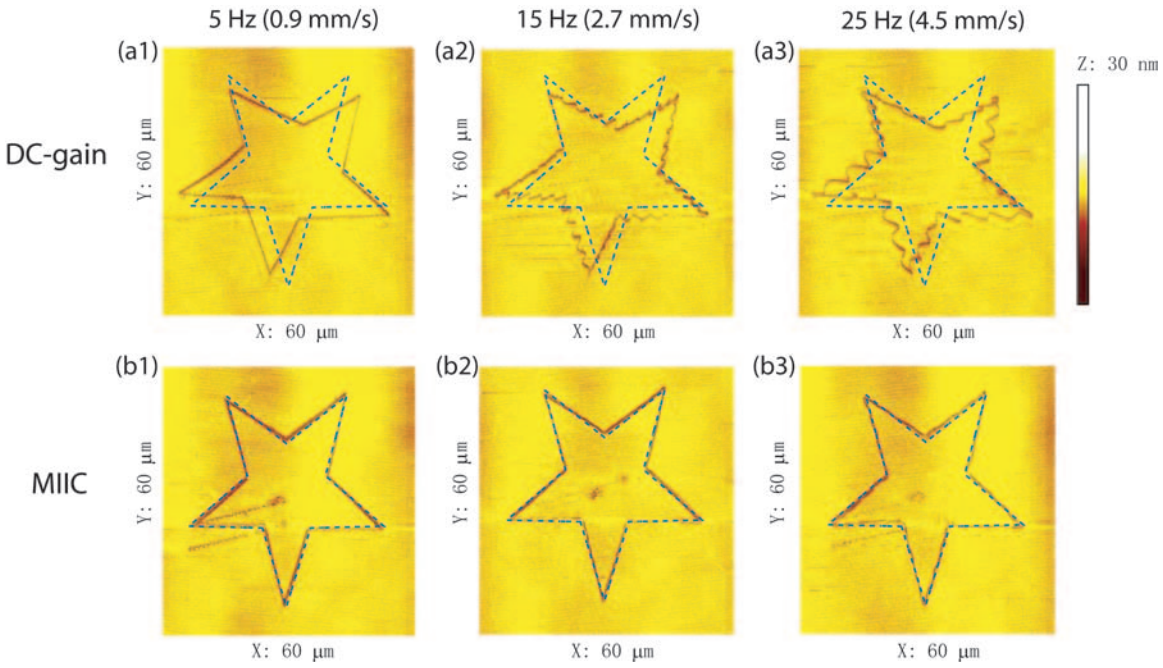

Figure 3.11 Comparison of the nanofabrication images of the continuous pentagram pattern obtained by using (top row) the DC-gain method with (bottom row) those obtained by using the MIIC technique at (a1, b1) 5 Hz, (a2, b2) 15 Hz, and (a3, b3) 25 Hz, respectively, where the corresponding average line speeds are given in the title, and the blue–dashed lines represent the desired pentagram pattern.

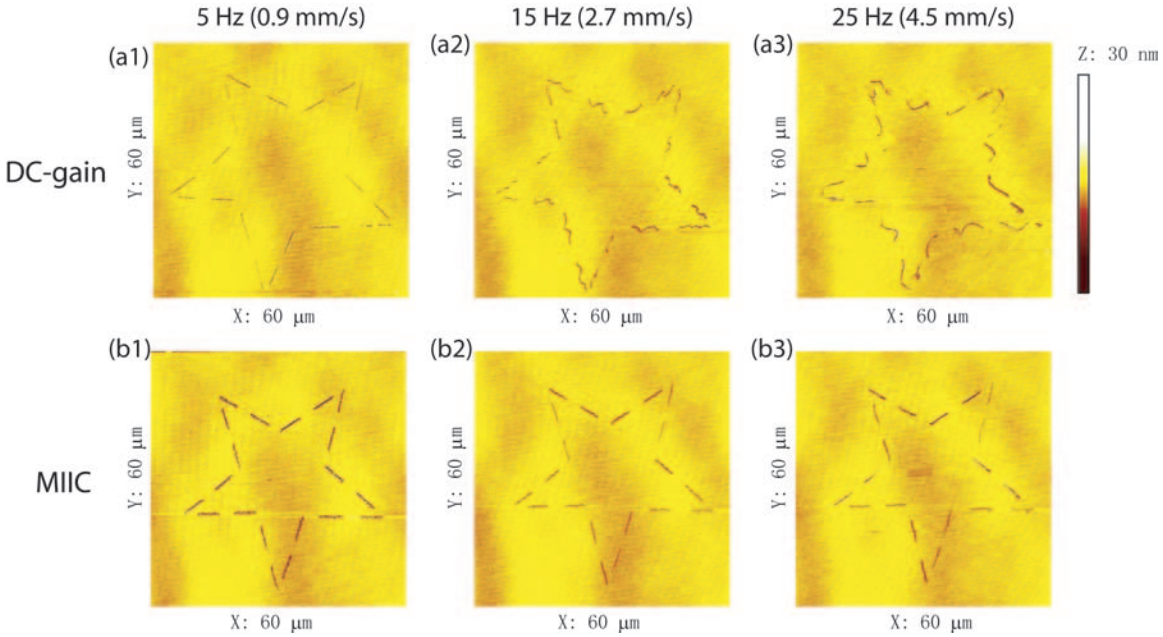

Figure 3.12 Comparison of the nanofabrication images of the dashed-line pentagram pattern obtained by (top row) using the DC-gain method with (bottom row) those obtained by using the MIIC technique at (a1, b1) 5 Hz, (a2, b2) 15 Hz, and (a3, b3) 25 Hz, respectively, where the corresponding average line speeds are given in the title.

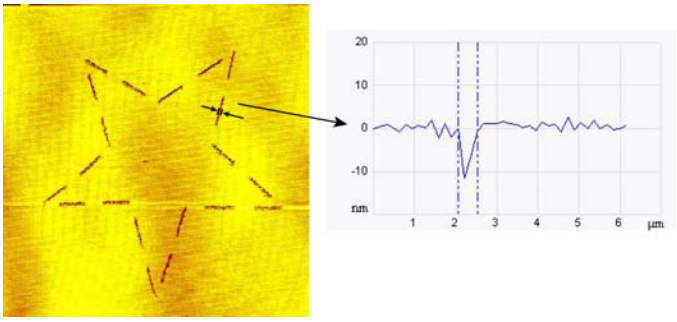

Figure 3.13 The cross section image of the dashed pentagram. The right image shows the depth of the fabricated groove

CHAPTER 4. CONCLUSION

This thesis has been focused on the compensation for the hardware adverse effects during high-speed large-range AFM operation. The hardware adverse effects include hysteresis, and vibration dynamics effects of the piezo actuator as well as the cross-axis coupling effect between the $x-y$and z axes. These adverse effects become more severe in high-speed large-range motion.

An integrated approach to high-speed AFM imaging of large-size samples is developed. The approach combines the enhanced inversion-based iterative control (EIIC) technique for lateral x-y axes scanning with a dual-stage piezo actuator for vertical z-axis positioning. The EIIC algorithm can effectively compensate for the nonlinear hysteresis and vibrational dynamics effects of piezotube actuator during high-speed, large-size lateral scanning. The dual-stage actuator combines a large-size piezo actuator of relatively low bandwidth with a small-size piezo actuator of high bandwidth, making it possible to obtain high-speed positioning at large displacement range. By using this integrated approach, the hardware adverse effects can be effectively compensated for, and AFM imaging in high-speed and large-range can be achieved.

In addition, an iterative control approach to achieve probe-based high-speed nanofabrication at large range is proposed. It was also shown that in AFM nanofabrication the model-less inversion-based iterative control (MIIC) technique can effectively compensate for the nonlinear hysteresis and vibrational dynamics effects of piezotube actuator, thereby improve the fabrication throughput. Also, the coupling compensation process developed by using the MIIC can successfully account for the coupling-caused disturbance from the lateral to the vertical motion. Therefore, the precision positioning can be achieved in all $x-y-z$ axes and high-speed large-range multi-axis AFM nanofabrication can be realized.

APPENDIX

MATLAB FILES

High-speed large-range AFM imaging

```
%================================================================
%PROGRAM NAME: Iteration_EIIC.m
%FUNCTION:  do the iteration in x-axis piezo actuator
%           and find the converged EIIC control for x axis.
%================================================================
%make connection between target-PC and host-PC
H_ftp=xpctarget.ftp('TCPIP','192.168.0.10','22222');%ftp
H_fsys=xpctarget.fs('TCPIP','192.168.0.10','22222');%file system
%The following part: empty 'h_output,dat'-x direction out
% generates a triangular input
N =2001;% the total number of the points
p =501; %the number of the points of half period
p_d=1000;
freq=10;
eff_frq_rto=0.12 ;%0.03(50Hz);0.15(10.3(5Hz)0Hz);
K = ceil(N/(2*p-2));
w = zeros(1,K*(2*p-2)+1);
rp = linspace(-1,1,p);
```

```
rn = linspace(1,-1,p);
r = [rp rn(2:p)];
for k = 1:K
w(1+(k-1)*(2*p-2):1+k*(2*p-2)) = r;
end
x = w(1:N);
y_d=4.65* x ;
y_desired =y_d(1:(2*p_d+1));
input=y_desired;
%input=y_desired./(-0.699); %DC gain x:0.6445; y:0.699
input_1=input(2:(2*p_d+1));
for jj=2:10
    input=[input,input_1];
end;
f_sample=freq*p_d;
setparam(tg,7,1/f_sample);
setparam(tg,14,1/f_sample);
setparam(tg,21,1/f_sample);
tg.SampleTime=1/f_sample;
tg.StopTime=length(input)/f_sample;
xpcbytes2file('white.dat',input);
H_ftp.put('white.dat');
try
    tg.start
catch
end
h=getlog(tg, 'OutputLog');
output=h((p_d*15+1):(p_d*17+1),1);
```

```
y_desired=y_desired';
input=input(1:(2*p_d+1))';
output=output;
input=Input_Compute_EIIC(y_desired,input,output,1,
eff_frq_rto,1/f_sample);
%duplicate input
for ii=1:10
 input_1=input(2:(2*p_d+1));
for jj=2:10
    input=[input;input_1];
end;
tg.StopTime=length(input)/f_sample;
xpcbytes2file('white.dat',input);
    H_ftp.put('white.dat');
try
    tg.start
catch
end
h=getlog(tg, 'OutputLog');
output=h((p_d*16+1):(p_d*18+1),1);
D_output=output-y_desired;
output=output-mean(D_output);
figure(1);subplot(211);plot((1:length(y_desired))./f_sample,
y_desired/9.3*50,(1:length(output))./f_sample,output/9.3*50);
title('DCgain output(desired)and output(k)(50Hz)');
legend('y_desired','output(k)','Location','SouthWest')
ylabel('Voltage(V)');xlabel('time(second)');
ylim([-30 30]); xlim([0 length(output)/f_sample]);
```

```
subplot(212);plot((1:length(y_desired))./f_sample,
(y_desired-output)/9.3*50);
title('error between output(desired) and output(k)');
ylabel('Voltage(V)');xlabel('time(second)');
xlim([0 length(output)/f_sample]);
ylim([-0.05 0.05]);
Error=max(abs(y_desired-output)/9.3*50)
input=input(1:(2*p_d+1));
input=Input_Compute_EIIC(y_desired,input,output,1,
eff_frq_rto,1/f_sample);
pause;
end
%%%%%%%%% Generate whole input for 128 periods %%%%%%%%%%%%%%%%%%%%
input_1=input(2:(2*p_d+1));
for kk=2:84
    input=[input;input_1];
end;
k_1=  linspace(0,input(1),(30*p_d-1));
k_2=  linspace(input(length(input)),0,20*p_d);
input= [k_1' ;input; k_2'];
figure(10);plot((1:length(input))./f_sample,input);
title('final input');
size(input)
y_desired_1=y_desired(2:(2*p_d+1));
for kk=2:74
    y_desired=[y_desired;y_desired_1];
end;
k_1=  linspace(0,y_desired(1),(10*p_d-1));
```

```
k_2=  linspace(y_desired(length(y_desired)),0,10*p_d);
y_desired= [k_1' ;y_desired; k_2'];
figure(11);plot((1:length(y_desired))./f_sample,y_desired);
title('y_desired');

%=================================================================
%PROGRAM NAME: freq_response.m
%FUNCTION: Compute the frequency response and the boundary of the
%          iterative coefficient.
%=================================================================
d1=load('X1040'); %the frequency response data coverted from the DSA
d2=load('X1060'); %the frequency response data coverted from the DSA
d3=load('X1080'); %the frequency response data coverted from the DSA
w1=d1.o2i1x;
w2=d2.o2i1x;
w3=d3.o2i1x;
g1=-d1.o2i1;
g2=-d2.o2i1;
g3=-d3.o2i1;
g1_ave=(g1+g2+g3)/3;
figure(1);subplot(211);
semilogx(w1,20*log10(abs(g1)),':g',...
    w2,20*log10(abs(g2)),'--b',...
    w3,20*log10(abs(g3)),'-.k',...
   w1,20*log10(abs(g1_ave)),'-r')
xlim([min(w1) max(w1)])
ylabel('Magnitude(db)');
xlabel('Frequency (Hz)');
```

```
title('Frequency Response');
subplot(212);
semilogx(w1,unwrap(angle(g1))*180/pi,':g',...
    w2,unwrap(angle(g2))*180/pi,'--b',...
    w3,unwrap(angle(g3))*180/pi,'-.k',...
    w1,unwrap(angle(g1_ave))*180/pi,'-r')
xlim([min(w1) max(w1)])
ylabel('Phase(degree)');
xlabel('Frequency (Hz)')
h=legend('40mv','60mv','80mv','average','Location','SouthWest');
set(h,'Interpreter','none')
%.....................................................
INF_M_g=(min(abs([g1./g2,g2./g1,g1./g3,g3./g1,g2./g3,g3./g2]')));
SUP_M_g=(max(abs([g1./g2,g2./g1,g1./g3,g3./g1,g2./g3,g3./g2]')));
rho_upperbound=2./SUP_M_g;
rho=0.5*rho_upperbound;
for ii=1:length(rho)
    if (rho(ii)>=1||rho(ii)<=0)
        rho(ii)=mean(rho);
    else rho(ii)=rho(ii);
    end
end
MIN_A_g=(min(angle([g1./g2,g2./g1,g1./g3,g3./g1,g2./g3,g3./g2]')));
Max_A_g=(max(angle([g1./g2,g2./g1,g1./g3,g3./g1,g2./g3,g3./g2]')));
rho_A_upperbound=2./Max_A_g;
rho_A=MIN_A_g;
figure(2);subplot(211);semilogx(w1,SUP_M_g,':',w1,rho_upperbound,'--',
w1,rho)
```

```
ylabel('Magnitude(db)');
xlabel('Frequency(Hz)');
xlim([10 2500])
subplot(212);semilogx(w1,Max_A_g*180/pi,':',w1,rho_A_upperbound*180/pi,
'--',w1,-rho_A*180/pi)
ylabel('Phase(degree)');xlabel('Frequency(Hz)')
xlim([10 2500])
legend('max\DeltaG(j\omega)','\rho_{sup}(\omega)','\rho(\omega)
selected','Location','NorthWest')
%.....................................................................
frq=w1;
g_ave=g1_ave;
save system frq g_ave
save rho rho

%=====================================================================
%PROGRAM NAME: Input_Compute_EIIC.m
%FUNCTION: Compute the new control input by using the enhanced
%          inversion-based iterative control (EIIC) algorithm.
%=====================================================================
%REQUIRED INPUT: y_desired: the desired output trajectory
%                input: the control input from last iteration
%                output: the system output from last iteration
%                periods: periods repeated from the calculation
%                eff_frq_rto: the ratio between the frequency range
%                             aimed to track and the measured
%                             frequency range in the dynamics model
%                dt: the sampling time
```

```
%=================================================================
function input=Input_Compute_EIIC(y_desired,input,output,periods,
eff_frq_rto,dt)
y_desired_new=y_desired;
len_input=length(input);
%%%%%%%%%%%%%%%%%%%%%%%%%%%%%%%%%%%%%%%%%%%%%%%%%%%%%%%%%%%%%%%%
% 1. Duplicate input, output and desired trajectory
%%%%%%%%%%%%%%%%%%%%%%%%%%%%%%%%%%%%%%%%%%%%%%%%%%%%%%%%%%%%%%%%
input_1=input(2:len_input);
output_1=output(2:len_input);
y_desired_1=y_desired_new(2:len_input);
for ii=2:periods
    input=[input;input_1];
    output=[output;output_1];
    y_desired_new=[y_desired_new;y_desired_1];
end
if periods==1
    input=input_1;
    output=output_1;
    y_desired_new=y_desired_1;
end
     ave_input=mean(input);
     ave_output=mean(output);
     ave_y_desired_new=mean(y_desired_new);
     input=input-ave_input;
    output=output-ave_output;
    y_desired_new=y_desired_new-ave_y_desired_new;
%%%%%%%%%%%%%%%%%%%%%%%%%%%%%%%%%%%%%%%%%%%%%%%%%%%%%%%%%%%%%%%%
```

```
% 2. Discrete Fast Fourier Transform
%%%%%%%%%%%%%%%%%%%%%%%%%%%%%%%%%%%%%%%%%%%%%%%%%%%%%%%%%%%%%%%%
U = fft(input);
Y=fft(output);
Y_d = fft(y_desired_new);
len_f=floor(length(U)/2)+1;% Number of Frequcncy component of
%input, output, desired tracking output after FFT transform
%%%%%%%%%%%%%%%%%%%%%%%%%%%%%%%%%%%%%%%%%%%%%%%%%%%%%%%%%%%%%%%%
% 3. Find new input
%%%%%%%%%%%%%%%%%%%%%%%%%%%%%%%%%%%%%%%%%%%%%%%%%%%%%%%%%%%%%%%%
len_H=floor(len_f*eff_frq_rto);
% Finding proper even or odd number for len_H depending on input
%data size
if length(U)/2==floor(length(U)/2)
    if len_H/2==floor(len_H/2)
        len_H=len_H-1;
        disp('Case 1')
    else
        disp('Case 2')
    end
else
    if len_H/2==floor(len_H/2)
        disp('Case 3')
    else
        disp('Case 4')
        len_H=len_H-1;
    end
end
```

```
%%%%%%%%%%%%%%%%%%%%%%%%%%%%%%%%%%%%%%%%%%%%%%%%%%%%%%%%%%%%%%%%
% Core input computation
% U_k+1(jw)=U_k(jw) / Y_k(jw) * Y_d(jw)
%%%%%%%%%%%%%%%%%%%%%%%%%%%%%%%%%%%%%%%%%%%%%%%%%%%%%%%%%%%%%%%%
    sm_out_idx=find(abs(Y(1:len_f))<10^-8);
%    G_pre=Y(1:len_f)./U(1:len_f);
scale=10^0;
rad=1;%2*pi;
lnth=len_input;
fD=1/dt*(0:floor(lnth/2))/lnth/scale;
% Sys ID with Large Amp (10mV), But This is small
load system  % contains: frq g_ave
%Frequency component of AFM
fs=frq*rad/scale;
%Frequency response component of AFM
sc=real(g_ave);
    max_fs=max(fs);
    I_max=max(find(fD<max_fs));
G_pre=transpose(interp1(fs,sc,fD(1:I_max)*rad, 'spline'));
%   figure(3);subplot(211);plot(fD(1:I_max),20*log10(abs()));
    %ylabel('Mag (dB))');title('Expected system dynamics')
    %subplot(212);plot(fD(1:I_max),unwrap(angle((G_pre))));
    %ylabel('Phase (rad)');
%pause
    new_u_half_pre=zeros(len_f,1);
    load rho
    rho=transpose(interp1(fs,rho,fD(1:I_max),'spline'));
%     close all
```

```
%     plot(fD(1:I_max),rho)
%     pause
Mag_n_half=abs(U(1:I_max))+rho.*abs(1./G_pre).*
(abs(Y_d(1:I_max))-abs(Y(1:I_max)));
Phs_n_half=angle(U(1:I_max))+(angle(Y_d(1:I_max))
-angle(Y(1:I_max)));
new_u_half_pre(1:I_max)=Mag_n_half.*(cos(Phs_n_half)
+i*sin(Phs_n_half));
new_u_half_pre(sm_out_idx)=zeros(size(sm_out_idx));
% Ignore small output frequency component
new_u_half_pre(len_H+1:len_f,1)=zeros(len_f-len_H,1);
% First Half size data from inversion
% new_u_half_pre(1)=new_u_half_pre(1)-length(Y)*
%((ave_y_desired_new-ave_output)/abs(G_pre(2)))+length(Y)*ave_input;
%%%%%%%%%%%%%%%%%%%%%%%%%%%%%%%%%%%%%%%%%%%%%%%%%%%%%%%%%%%%
% 4. Input Generation for one period
%%%%%%%%%%%%%%%%%%%%%%%%%%%%%%%%%%%%%%%%%%%%%%%%%%%%%%%%%%%%
if length(U)/2==floor(length(U)/2)
    new_u_half_post=conj(flipud(new_u_half_pre));
% Second half size data
    new_u=[new_u_half_pre ;new_u_half_post(2:len_f-1)];
% Combining First and second half size data
    new_input=real(ifft(new_u));
% Generation new multiple periods of input in real value
else
    new_u_half_post=conj(flipud(new_u_half_pre));
% Second half size data
    new_u=[new_u_half_pre ;new_u_half_post(1:len_f-1)];
```

```
% Combining First and second half size data
    new_input=real(ifft(new_u));
% Generation new multiple periods of input in real value
end
    if periods==1
        input=[new_input(length(new_input));new_input];
    else
        input=new_input((len_input-1)*floor(periods/2):(len_input-1)
        *floor(periods/2)+1));
% Picking one representing input period
    end
% figure(4);plot(input);title('input2');hold off;

%=================================================================
%PROGRAM NAME: PIcontroller.m
%FUNCTION: design the PI controller.
%=================================================================
freq=100;
f_sample=freq*1000;
kp=1;Ti=60;
p=1;
skp=tf([kp*200*p*pi],[1 200*p*pi]);
ski=tf([Ti*kp*20*p*pi],[1 20*p*pi]);
k=-(skp+ski);
w=6130;d=0.05;c=1;
f=tf([1 2*d/c*w w^2],[1 2/c*w w^2])
[b,a]=butter(1,400/500);
filter=tf(b,a);
```

```
%figure(10);bode(s,'g');hold on; bode(s*f,'r')
d_model=load('sys_model');
s=d_model.s;
ss=feedback(k*f*s,1);
figure(2);bode(ss,'k');hold on;
sys=c2d(f*k,1/f_sample);
[num,den]=tfdata(sys);
% [num,den]=tfdata(sys,'v');
sys_s=c2d(s,1/f_sample);
[num_s,den_s]=tfdata(sys_s);
ee=feedback(1,f*k*s);
figure(2);bode(ee,'r');bode(k);
figure(1);step(ss);
d=load('x_output_desired');
input=d.input;
% f_sample=50000;
[y,t]=lsim(ss,input,(1:length(input))/f_sample);
range=1:length(input);%f_sample*1+1:f_sample*2;
figure(3);plot(t(range),y(range));hold on;plot(t(range),
input(range),'r');
%=================================================================
%PROGRAM NAME: plot_image.m
%FUNCTION: plot the 3D image by using the AFM imaging data .
%=================================================================
% h=getlog(tg, 'OutputLog');
% output=h(:,1);
output=d.output;
z_data=output*(200/0.8);
```

```
 %r_1=39650;
%z_data=d2.output*(200/3);
%d_1=load('Z_10Hz')
%z_data=d_1.z_data_10Hz;
% f_sample=8000;
%   f_filt=1000;
%   [b,a]=butter(4,20000/f_sample);
%   z_data = filtfilt(b,a,z_data);
M=1000;
N=128;
t=500;
start_p=30000;
%start_p=15597;
x_row=((-(t-1)/2:1:(t-1)/2)/((t-1)/2)+1)*25;
y_col=((-(N-1)/2:1:(N-1)/2)/((N-1)/2)+1)*25;
[xdat,ydat]=meshgrid(x_row,y_col);
% xdat=reshape1(x_data,M,N,t,3000);
% ydat=reshape1(y_data,M,N,t,3000);
% z_col(1:200)=ones(1,200);
% z_col(50:100)=0.*z_col(50:100);
% z_col(150:200)=0.*z_col(150:200);
% for i=1:N
%     zdat(i,:)=z_col';
% end;
% zdat(50:100,:)=0*zdat(50:100,:);
% zdat(150:200,:)=0*zdat(150:200,:);
 zdat1=reshape(z_data(start_p+1:start_p+M*N,1),M,N);
%zdat1=reshape(z_data(30000+1:30000+M*N,1),M,N);
```

```
zdat=zdat1(1:t,:);
zdat=zdat';
%ydat=flipud(ydat);  % uncomment to make image match Burleigh's
LineRemove=1;
[Z_Row, Z_Col] = size(zdat);
clear Z_Shift;
for jj = 1:Z_Row
   [p_z(jj,:), s] = polyfit(xdat(1,:), zdat(jj,:), 1);
if(LineRemove)
   Z_Tilt0 = p_z(jj,1)*xdat(1,:) + p_z(jj,2);
   Z_Shift(jj,:) = zdat(jj,:) - Z_Tilt0;
end
end
if(~LineRemove)
  p_z_m = [mean(p_z(:,1)), mean(p_z(:,2))];
  for jj = 1:Z_Row
     Z_Tilt(jj,:) = p_z_m(1)*xdat(1,:) + p_z_m(2);
  end
  Z_Shift = zdat - Z_Tilt;
end
Scale_Coef=0.5;
Z_Shift = Z_Shift.*Scale_Coef;
Cut_Ratio=.6;
Z_Shift_F = Z_Shift;%Win_Filter(Z_Shift, Cut_Ratio);
B_beta=[0.5,0.6];
Dis_Axis = [min(min(xdat)), max(max(xdat)), min(min(ydat)),
max(max(ydat))];
color='hot';
```

```
colormap(color);
cmap=colormap;
colornew1=brighten(cmap, B_beta(1));
colornew2=brighten(cmap, B_beta(2));
Fig_No=1;
figure(Fig_No);
surface(xdat, ydat, Z_Shift_F, 'EdgeColor', 'none');
colormap(colornew2);
axis(Dis_Axis);
axis square
ylabel('y-axis displacement(\mum)');
xlabel('x-axis displacement(\mum)')
return;
[Yd,N_period]=Sawtoothwave(4000,10,1.6040*5,0,5);
figure(11),plot(z_data(3000+400*10+1:3000+400*11,1),'r'),hold on;
figure(11),plot(-Yd,'b');
figure(12),plot(z_data(:,1),'r');hold on;
figure(12),plot(z_data(:,2),'b');
```

High-speed large-range AFM nanofabrication

```
%================================================================
%PROGRAM NAME: Iteration_MIIC.m
%FUNCTION: do the iteration in all x-y-z axes piezo actuators
%          simultaneously and find the converged MIIC control
%          for x-y-z axes.
%================================================================
format short
%make connection between target-PC and host-PC
```

```
H_ftp=xpctarget.ftp('TCPIP','192.168.0.10','22222');%ftp
H_fsys=xpctarget.fs('TCPIP','192.168.0.10','22222');%file system
p_d=1000;%per the whole star ------for the highfreq p_d=1000
freq=5; %frequecy for the whole star
f_sample=freq*p_d;
eff_frq_rto_x=0.05; %2hz:1; 10hz:0.5; 30hz: 0.04; 40hz:0.04;
eff_frq_rto_y=0.05;
eff_frq_rto_z=1;
ratio=1;
ramp_p=3;
%%%%%%%%%% Load desired signal %%%%%%%%%%%%%%%%%%%%%%%%%%%%%%
d_x=load('star_x_dc');
x_desired=d_x.xinput_d*ratio*0.615;
xinput=-x_desired;
ramp_0=linspace(0,0,ramp_p*p_d);
ramp_1=linspace(0, xinput(1),ramp_p*p_d);
ramp_2=linspace(xinput(length(xinput)),0,ramp_p*p_d);
xinput=[ramp_0 ramp_1 xinput ramp_2];
d_y=load('star_y_dc');
y_desired=d_y.yinput_d*ratio*0.65;
yinput=-y_desired;
ramp_0=linspace(0,0,ramp_p*p_d);
ramp_1=linspace(0, yinput(1),ramp_p*p_d);
ramp_2=linspace(yinput(length(yinput)),0,ramp_p*p_d);
yinput=[ramp_0 ramp_1 yinput ramp_2];
 f_filt=0.15*f_sample;
[b,a]=butter(6,f_filt/f_sample);
y_desired= filtfilt(b,a,y_desired);
```

```
d_z=load('star_z_dc');
z_desired=(d_z.zinput_d)*1;
%%%%%%%%% Find the new z def desired trajectory %%%%%%%%%%%%%%%
d_z_xy=load('z_def_5hz');
z_desired_xy=d_z_xy.zoutput;
ave_z_desired_xy=mean(z_desired_xy);
z_desired_xy=z_desired_xy-ave_z_desired_xy;
f_filt=0.03*f_sample;
[b,a]=butter(4,f_filt/f_sample);
z_desired_xy= filtfilt(b,a,z_desired_xy);
figure(100); plot(z_desired_xy);
z_desired=z_desired-z_desired_xy';
f_filt=0.4*f_sample;
[b,a]=butter(1,f_filt/f_sample);
z_desired= filtfilt(b,a,z_desired);
z_desired=z_desired;
%.....................................................
ramp_0=linspace(0,0,ramp_p*2*p_d);
ramp_1=linspace(0,0,ramp_p*p_d);
zinput=[ramp_0 z_desired ramp_1];
zinput=-zinput/1.53; %%DC gain(z sensor):-0.57;deflection:-1.58
figure(1);plot(z_desired); hold on; plot(zinput,'r');
t_vector=(1:length(xinput));
t_1p=((25*p_d+1):(26*p_d));
t_star=2*ramp_p*p_d+1:2*ramp_p*p_d+length(x_desired);
tg.SampleTime=1/f_sample;
tg.StopTime=length(xinput)/f_sample;
%%%%%%%% Get first output %%%%%%%%%%%%%%%%%%%%%%%%%%%%%%%%%%%%
```

```
xpcbytes2file('white_x.dat',xinput);
H_ftp.put('white_x.dat');
xpcbytes2file('white_y.dat',yinput);
H_ftp.put('white_y.dat');
xpcbytes2file('white_z.dat',zinput);
H_ftp.put('white_z.dat');
% figure(1);plot(xinput,yinput)
try
    tg.start
catch
end
h=getlog(tg, 'OutputLog');
h=h(t_star,:);
f_filt=0.8*f_sample;
[b,a]=butter(4,f_filt/f_sample);
h(:,:)= filtfilt(b,a,h(:,:));
xoutput=h(:,1);
youtput=h(:,2);
zoutput=h(:,3);
xinput=xinput(t_star)';
yinput=yinput(t_star)';
zinput=zinput(t_star)';
x_desired=x_desired';
y_desired=y_desired';
z_desired=z_desired';
%%%%%%%%%%%%%%%%%%%%%%% MIIC %%%%%%%%%%%%%%%%%%%%%%%%%%
for ii=1:10;
xinput=Input_Compute_MIIC_X(x_desired,xinput,xoutput,10,
```

```
eff_frq_rto_x,1/f_sample);
yinput=Input_Compute_MIIC_Y(y_desired,yinput,youtput,10,
eff_frq_rto_y,1/f_sample);
zinput=Input_Compute_MIIC_Z(z_desired,zinput,zoutput,1,
eff_frq_rto_z,1/f_sample);
%%%%% Add Ramp for input %%%%%%%%%%%%%%%%%%%%%%%%
xinput=[linspace(0,0,ramp_p*p_d)';linspace(0, xinput(1),ramp_p*p_d)';
xinput;linspace(xinput(length(xinput)),0,ramp_p*p_d)'];
yinput=[linspace(0,0,ramp_p*p_d)';linspace(0, yinput(1),ramp_p*p_d)';
yinput;linspace(yinput(length(yinput)),0,ramp_p*p_d)'];
zinput=[linspace(0,0,2*ramp_p*p_d)';zinput;linspace(0,0,ramp_p*p_d)'];
xpcbytes2file('white_x.dat',xinput);
H_ftp.put('white_x.dat');
xpcbytes2file('white_y.dat',yinput);
H_ftp.put('white_y.dat');
xpcbytes2file('white_z.dat',zinput);
H_ftp.put('white_z.dat');
try
    tg.start
catch
end
h=getlog(tg, 'OutputLog');
h=h(t_star,:);
f_filt=0.8*f_sample;
[b,a]=butter(4,f_filt/f_sample);
h(:,:)= filtfilt(b,a,h(:,:));
%%%remove offset%%%%%%%%%
xoutput=h(:,1);
```

```
D_xoutput=xoutput-x_desired;
xoutput=xoutput-mean(D_xoutput);
youtput=h(:,2);
D_youtput=youtput-y_desired;
youtput=youtput-mean(D_youtput);
zoutput=h(:,3);
D_zoutput=zoutput-z_desired;
zoutput=zoutput-mean(D_zoutput);
xinput=xinput(t_star);
yinput=yinput(t_star);
zinput=zinput(t_star);
%%%%%%%%% Plot output VS desired output %%%%%%%%%%%%%%%%%%
t_plot=1:length(xoutput);
figure(4);subplot(211);plot(t_plot./f_sample,x_desired,
t_plot./f_sample,xoutput);
title('xoutput(desired)and xoutput(k)');
legend('x_desired','xoutput(k)','Location','SouthWest')
ylabel('Voltage(V)');xlabel('time(second)');
xlim([0 length(xoutput)/f_sample]);
subplot(212);plot((t_plot)./f_sample,x_desired-xoutput);
title('error between xoutput(desired) and xoutput(k)');
ylabel('Voltage(V)');%xlabel('time(second)');
xlim([0 length(youtput)/f_sample]);
figure(5);subplot(211);plot((t_plot)./f_sample,y_desired,
(t_plot)./f_sample,youtput);
title('youtput(desired)and youtput(k)');
legend('y_desired','youtput(k)','Location','SouthWest')
ylabel('Voltage(V)');xlabel('time(second)');
```

```
xlim([0 length(youtput)/f_sample]);
subplot(212);plot((t_plot)./f_sample,y_desired-youtput);
title('error between youtput(desired) and youtput(k)');
ylabel('Voltage(V)');
xlim([0 length(youtput)/f_sample]);
figure(6);subplot(211);plot((t_plot)./f_sample,z_desired,
(t_plot)./f_sample,zoutput);
title('zoutput(desired)and zoutput(k)');
legend('z_desired','zoutput(k)','Location','SouthWest')
ylabel('Voltage(V)');xlabel('time(second)');
xlim([0 length(zoutput)/f_sample]); ylim([-3 8]);
subplot(212);plot((t_plot)./f_sample,z_desired-zoutput);
title('error between zoutput(desired) and zoutput(k)');
ylabel('Voltage(V)');
xlim([0 length(zoutput)/f_sample]);
figure(8); plot((t_plot)./f_sample,zoutput);
title('deflection signal (coupling)');
legend('z_desired','zoutput(k)','Location','SouthWest')
ylabel('Voltage(V)');xlabel('time(second)');
xlim([0 length(zoutput)/f_sample]);
Error_max_x=max(abs(x_desired(2000:length(xoutput))
-xoutput(2000:length(xoutput))))/(max(x_desired)-min(x_desired))
Error_rms_x=norm(x_desired-xoutput)/sqrt(length(xoutput))
/(max(x_desired)-min(x_desired))
Error_max_y=max(abs(y_desired(2000:length(youtput))
-youtput(2000:length(youtput))))/(max(y_desired)-min(y_desired))
Error_rms_y=norm(y_desired-youtput)/sqrt(length(youtput))
/(max(y_desired)-min(y_desired))
```

```
Error_max_z=max(abs(z_desired(2000:length(zoutput))
-zoutput(2000:length(zoutput))))/(max(z_desired)-min(z_desired))
Error_rms_z=norm(z_desired-zoutput)/sqrt(length(zoutput))
/(max(z_desired)-min(z_desired))
lnth=length(xinput);
figure(7); plot(-x_desired(2*p_d+1:lnth),-y_desired(2*p_d+1:lnth),
-xoutput(2*p_d+1:lnth),-youtput(2*p_d+1:lnth));
legend('desired xy','output xy','Location','Southwest');
pause;
end;
return
%%%%%%%% Step #1 save data %%%%%%%%%%%%%%%%%%%%%%%%
xinput=[linspace(0, xinput(1),ramp_p*p_d)'; xinput;
linspace(xinput(length(xinput)),0,ramp_p*p_d)'];
yinput=[linspace(0, yinput(1),ramp_p*p_d)'; yinput;
linspace(yinput(length(yinput)),0,ramp_p*p_d)'];
save xinput_15hz_c xinput
save yinput_15hz_c yinput
save track_xy_5hz xoutput x_desired youtput y_desired
save z_def_5hz zoutput
%%%%%%%% Step #2 save data%%%%%%%%%%%%%%%%%%%%%%%%
xinput=[linspace(0, xinput(1),ramp_p*p_d)'; xinput;
linspace(xinput(length(xinput)),0,ramp_p*p_d)'];
yinput=[linspace(0, yinput(1),ramp_p*p_d)'; yinput;
linspace(yinput(length(yinput)),0,ramp_p*p_d)'];
save xinput_5hz_c xinput
save yinput_5hz_c yinput
zinput=[linspace(0, 0,ramp_p*p_d)'; zinput;
```

```
linspace(0,0,ramp_p*p_d)'];
save zinput_5hz_c zinput
save track_z_5hz_ zoutput z_desired

%================================================================
%PROGRAM NAME: Input_Compute_EIIC.m
%FUNCTION: Compute the new control input by using the model-less
%          inversion-based iterative control (MIIC) algorithm.
%================================================================
%REQUIRED INPUT: y_desired: the desired output trajectory
%                input: the control input from last iteration
%                output: the system output from last iteration
%                periods: periods repeated from the calculation
%                eff_frq_rto: the ratio between the frequency range
%                aimed to track and the measured frequncy range
%                in the dynamic model
%                dt: the sampling time
%================================================================
function input=Input_Compute_MIIC(y_desired,input,output,periods,
eff_frq_rto,dt)
y_desired_new=y_desired;
len_input=length(input);
%%%%%%%%%%%%%%%%%%%%%%%%%%%%%%%%%%%%%%%%%%%%%%%%%%%%%%%%%%%%%%%
% 1. Duplicate input, output and desired trajectory
%%%%%%%%%%%%%%%%%%%%%%%%%%%%%%%%%%%%%%%%%%%%%%%%%%%%%%%%%%%%%%%
input_1=input(2:len_input);
output_1=output(2:len_input);
y_desired_1=y_desired_new(2:len_input);
```

```
for ii=2:periods
    input=[input;input_1];
    output=[output;output_1];
    y_desired_new=[y_desired_new;y_desired_1];
end
if periods==1
    input=input_1;
    output=output_1;
    y_desired_new=y_desired_1;
end
ave_input=mean(input);
ave_output=mean(output);
ave_y_desired_new=mean(y_desired_new);
input=input-ave_input;
output=output-ave_output;
y_desired_new=y_desired_new-ave_y_desired_new;
%%%%%%%%%%%%%%%%%%%%%%%%%%%%%%%%%%%%%%%%%%%%%%%%%%%%%%%%%%%%%%%%%%%%%%%
% 2. Discrete Fast Fourier Transform
%%%%%%%%%%%%%%%%%%%%%%%%%%%%%%%%%%%%%%%%%%%%%%%%%%%%%%%%%%%%%%%%%%%%%%%
U = fft(input);
Y=fft(output);
Y_d = fft(y_desired_new);
G=Y./U;
len_f=floor(length(U)/2)+1;% Number of Frequcncy component of input,
output, desired tracking output after FFT transform
%%%%%%%%%%%%%%%%%%%%%%%%%%%%%%%%%%%%%%%%%%%%%%%%%%%%%%%%%%%%%%%%%%%%%%%
% 3. Find new input
%%%%%%%%%%%%%%%%%%%%%%%%%%%%%%%%%%%%%%%%%%%%%%%%%%%%%%%%%%%%%%%%%%%%%%%
```

```
len_H=floor(len_f*eff_frq_rto);
% Size of data to be used in inversion. Specific value
%(eff_frq_rto < 1) can be adjusted by user.
% Finding proper even or odd number for len_H
%depending on input data size
if length(U)/2==floor(length(U)/2)
    if len_H/2==floor(len_H/2)
        len_H=len_H-1;
        disp('Case 1')
    else
        disp('Case 2')
    end
else
    if len_H/2==floor(len_H/2)
        disp('Case 3')
    else
        disp('Case 4')
        len_H=len_H-1;
    end
end
%%%%%%%%%%%%%%%%%%%%%%%%%%%%%%%%%%%%%%%%%%%%%%%%%%%%%%%%%%%%%%%%%%%%%%%
% Core input computation
% U_k+1(jw)=U_k(jw) / Y_k(jw) * Y_d(jw)
%%%%%%%%%%%%%%%%%%%%%%%%%%%%%%%%%%%%%%%%%%%%%%%%%%%%%%%%%%%%%%%%%%%%%%%
sm_out_idx=find(abs(Y(1:len_f))<10^-8);
G_pre=Y(1:len_f)./U(1:len_f);
lnth=len_input;
fD=1/dt*(0:floor(lnth/2))/lnth;
```

```
figure(3);subplot(211);plot(fD(1:len_f),20*log10(abs(G_pre)),'*');
ylabel('Mag (dB))');
title('Expected system dynamics')
subplot(212);plot(fD(1:len_f),unwrap(angle((G_pre))));
ylabel('Phase (rad)');
new_u_half_pre=1./G_pre.*Y_d(1:len_f);% First Half size
%data from inversion
new_u_half_pre(sm_out_idx)=zeros(size(sm_out_idx));
% Ignore small output frequency component
new_u_half_pre(len_H+1:len_f,1)=zeros(len_f-len_H,1);
% First Half size data from inversion
x=2:10;
y=abs(G_pre(2:10));
%%%%%%%%%%%%%%%%%%%%%%%%%%%%%%%%%%%%%%%%%%%%%%%%%%%%%%%%%%%%%%%%%%%%
% 4. Input Generation for one period
%%%%%%%%%%%%%%%%%%%%%%%%%%%%%%%%%%%%%%%%%%%%%%%%%%%%%%%%%%%%%%%%%%%%
if length(U)/2==floor(length(U)/2)
    disp('Even')
    new_u_half_post=conj(flipud(new_u_half_pre));
    % Second half size data
    new_u=[new_u_half_pre ;new_u_half_post(2:len_f-1)];
    % Combining First and second half size data
    new_input=real(ifft(new_u));
    % Generation new multiple periods of input in real value
else
    disp('Odd')
    new_u_half_post=conj(flipud(new_u_half_pre));
    % Second half size data
```

```
    new_u=[new_u_half_pre ;new_u_half_post(1:len_f-1)];
    % Combining First and second half size data
    new_input=real(ifft(new_u));
    % Generation new multiple periods of input in real value
end
   if periods==1
        input=[new_input(length(new_input));new_input];
    else
        input=new_input((len_input-1)*floor(periods/2)
        :(len_input-1)*(floor(periods/2)+1));
        % Picking one representing input period
    end
%     figure(1);plot(input);title('Input signal')

%================================================================
%PROGRAM NAME: star_drawing.m
%FUNCTION: generate the x, y, z axes desired trajectories of
%          a dashed-line pentagram pattern.
%================================================================
HRadium=5;LRadium=2;
angle=18;radian=pi/180;
p=11; times=29;
m=100;
for i=1:p
    if rem(i,2)==1 %odd number
        xtrack(i)=HRadium*cos((angle+36*(i-1))*radian);
        ytrack(i)=HRadium*sin((angle+36*(i-1))*radian);
    else  %even number
```

```
        xtrack(i)=LRadium*cos((angle+36*(i-1))*radian);
        ytrack(i)=LRadium*sin((angle+36*(i-1))*radian);
    end
end
x_1=linspace(xtrack(1),xtrack(2),m);
x_2=linspace(xtrack(2),xtrack(3),m);
x_3=linspace(xtrack(3),xtrack(4),m);
x_4=linspace(xtrack(4),xtrack(5),m);
x_5=linspace(xtrack(5),xtrack(6),m);
x_6=linspace(xtrack(6),xtrack(7),m);
x_7=linspace(xtrack(7),xtrack(8),m);
x_8=linspace(xtrack(8),xtrack(9),m);
x_9=linspace(xtrack(9),xtrack(10),m);
x_10=linspace(xtrack(10),xtrack(11),m);
xinput=[x_1 x_2 x_3 x_4 x_5 x_6 x_7 x_8 x_9 x_10];
y_1=linspace(ytrack(1),ytrack(2),m);
y_2=linspace(ytrack(2),ytrack(3),m);
y_3=linspace(ytrack(3),ytrack(4),m);
y_4=linspace(ytrack(4),ytrack(5),m);
y_5=linspace(ytrack(5),ytrack(6),m);
y_6=linspace(ytrack(6),ytrack(7),m);
y_7=linspace(ytrack(7),ytrack(8),m);
y_8=linspace(ytrack(8),ytrack(9),m);
y_9=linspace(ytrack(9),ytrack(10),m);
y_10=linspace(ytrack(10),ytrack(11),m);
yinput=[y_1 y_2 y_3 y_4 y_5 y_6 y_7 y_8 y_9 y_10];
figure(1);plot(xinput,-yinput)
%generate z dash input signal
```

```
setpt=0;
press=6;
z_1=linspace(setpt,setpt,0.15*m);
z_2=linspace(setpt,press,0.05*m);
z_3=linspace(press,press,0.25*m);
z_4=linspace(press,setpt,0.05*m);
zinput=[z_1 z_2 z_3 z_4];
% z_1=linspace(0,0,50);
% z_2=linspace(press,press,50);
% zinput=[z_1 z_2];
zinput_1=zinput;
for k=1:19;
    zinput=[zinput zinput_1];
end;
% zinput=[zinput zinput(length(zinput):-1:1)];
figure(2);plot(zinput)
xinput_1=xinput;
for k=1:times; %20 periods
xinput=[xinput xinput_1];
end;
xinput_d=xinput/5*2.5*1.75/0.615; %for HRadium=25 um
xinput_d=xinput_d-mean(xinput_d);
yinput_1=yinput;
for k=1:times;
yinput=[yinput yinput_1];
end;
yinput_d=yinput/5*2.5*1.85/0.65; %for HRadium=25 um
yinput_d=yinput_d-mean(yinput_d);
```

```
zinput_1=zinput;
zinput=zeros(1,10*m);
for k=1:times;
    zinput=[zinput zinput_1];
end;
zinput_d=zinput;
% f_filt=0.3*f_sample;
% [b,a]=butter(1,f_filt/f_sample);
% zinput_d= filtfilt(b,a,zinput_d);
save star_x_dc xinput_d
save star_y_dc yinput_d
save star_z_dc zinput_d
```

BIBLIOGRAPHY

[1] S. Tien, Q. Zou, and S. Devasia, "Iterative control of dynamics-coupling-caused errors in piezoscanners during high-speed AFM operation," *IEEE Trans. on Control Systems Technology*, vol. 13, no. 6, pp. 921–931, 2005.

[2] K. Kim, Q. Zou and C. Su "A New approach to scan-trajectory design and track: AFM force measurement example," *ASME Journal of Dynamic Systems, Measurement and Control*, Vol. 130, pp. 051005-1–051005-10, 2008.

[3] K. S. Kim and Q. Zou, "Model-less inversion-based iterative control for output tracking: Piezoelectric actuator example," in *acc*, (Seattle, Washington, USA), 2008.

[4] G. K. Binning, C. F. Quate, C. Gerber, "Atomic foce microscopy," *Physical Review Letters*, vol. 56, pp. 930-933, 1986.

[5] D. Croft, G. Shedd, S. Devasia, "Creep, Hysteresis, and Vibration Compensation for Piezoactuators: Atomic Force Microscopy Application," *ASME Journal of Dynamic Systems, Measurement and Control*, vol. 123, pp. 35-43, 2001.

[6] M. J. Rost, D. A. Quist and J.W.M. Frenken, "Grains, Growth, and Grooving," *Physical Review Letters*, vol. 91, pp. 026101, 2003.

[7] P. G. Vekilov, "Self-assembly of apoferritin molecules into crystals: thermodynamics and kinetics of molecular level processes," *Physical Review Letters*, vol. 45, pp. 175-199, 2002.

[8] C. Rotsch, K. Jacobson, and M. Radmacher, "Dimensional and mechanical dynamics of active and stable edges in motile fibroblasts investigated by using atomic force microscopy," *Cell Biology*, vol. 96, pp. 9956-9963, 1999.

[9] H. Lin, D. O. Clegg, and R. Lal, "Imaging Real-Time Proteolysis of Single Collagen I Molecules with an Atomic Force Microscope," *Biochemistry*, vol. 38, pp. 921-926, 1999.

[10] J. K. H. Hörberl, and M. J. Miles, "Scanning Probe Evolution in Biology," *Science*, vol. 302, pp. 1002-1005, 2003.

[11] N. J. Curson, R. Nemutudi, N. J. Appleyard, M. Pepper, D. A. Ritchie, and G. A. C. Jones, "Ballistic transport in a GaAs/AlxGa1CxAs one-dimensional channel fabricated using an atomic force microscope," *Microelectron*, vol. 31, no. 15, pp. 1244–1245, 1995.

[12] R. Magno and B. R. Bennett, "Nanostructure patterns written in $iii - v$ semiconductors by an atomic force microscope," *Appl. Phys. Lett.*, vol. 70, p. 1855, April, 1997.

[13] J. Michler, R. Gassilloud, P. Gasser, L. Santinacci, and P. Schmukib, "Defect-free AFM scratching at the si/sio_2 interface used for selective electrodeposition of nanowires," *Electrochem. Solid-State Lett.*, vol. 7, pp. A41–A43, 2004.

[14] R. D. Piner, J. Zhu, F. Xu, S. Hong, and C. A. Mirkin, "Dip-Pen nanolithography," *Science*, vol. 283, no. 5402, pp. 661–663, 1999.

[15] P. Vettiger, G. Cross, M. Despont, U. Drechsler, U. Durig, B. Gotsmann, W. Haberle, M. A. Lantz, H. E. Rothuizen, R. Stutz, and G. K. Binnig, "The millipede - nanotechnology entering data storage," *IEEE*, vol. 1, pp. 39–55, 2002.

[16] D. A. Bristow, M. Tharayil, A. G. Alleyne, "A survey of iterative learning control," *Control Systems Magazine, IEEE*, Vol. 26, pp. 96-114, 2006

[17] M. Verwoerd, G. Meinsma, T. de Vries, "On admissible pairs and equivalent feedback – Youla parameterization in iterative learning control," *Automatica*, vol. 42, pp. 2079-2089, 2006.

[18] S. Salapaka, A. Sebastian, J. P. Cleveland, and M. V. Salapaka , "High bandwidth nano-positioner: A robust control approach," *Review of Scientific Instruments*, vol. 73(9), pp. 3232, 2002.

[19] G. Schitter, P. Menold, H.F. Knapp, F. Allgower, and A. Stemmer, "High performance feedback for fast scanning atomic force microscopes," *Review of Scientific Instruments*, vol. 72, pp. 3320, 2001.

[20] L. Qiu and E. J. Davison, "Performance Limitations of Non-minimum Phase Systems in the Servomechanism Problem," *Automatica*, vol. 29, pp. 337, 1993.

[21] S. Devasia, D. Chen, B. Paden, "Nonlinear Inversion-Based Output Tracking," *IEEE Trans. on Automatic Control*, vol. 41, pp. 930, 1996.

[22] Y. Wu and Q. Zou, "Iterative control approach to compensate for the hysteresis and the vibrational dynamics effects of piezo actuators," *IEEE Trans. on Control Systems Technology*, vol. 15, pp. 936–944, 2007.

[23] A. Sebastian and S. M. Salapaka, "Design methodologies for robust nano-positioning," *IEEE Trans. on Control Systems Technology*, vol. 13, no. 6, pp. 868–876, 2005.

[24] S. Hu and A. Raman, "Chaos in atomic force microscopy," *Physical Review Letters*, vol. 96, no. 3, pp. 0361072, 2006.

[25] A. Khurshudov, K. Kato, and H. Koide, "Wear of the AFM diamond tip sliding against silicon," *WEAR*, vol. 203, pp. 22-27, 1997.

[26] M. Radmacher, "Measuring the Elastic Properties of Biological Samples with the AFM," *IEEE Engineering in Medicine and Biology Magazine*, vol. 16, pp. 47-57, 1997.

[27] T. Ando, N. Kodera, E. Takai, D. Maruyama, K. Saito, and A. Toda, "A high-speed atomic force microscope for studying biological macromolecules," *Proceedings of the National Academy of Sciences of the USA*, vol. 98(22), pp. 12468-12472, Oct., 2001.

[28] M. J. Rosta, L. Crama, P. Schakel, E. van Tol and G. B. E. M. van Velzen-Williams and C. F. Overgauw, H. ter Horst and H. Dekker, B. Okhuijsen, M. Seynen, A. Vijftigschild, P. Han, A. J. Katan, K. Schoots, R. Schumm, W. van Loo, T. H. Oosterkamp and J. W. M. Frenken, "Scanning probe microscopes go video rate and beyond," *Review of Scientific Instruments*, vol. 76, pp. 53710, 2005.

[29] A. D. L. Humphris and J. K. Hobbs and M. J. Miles, "Ultra high-speed scanning near-field optical microscopy capable of over 100 frames per second," *Applied Physics Letters*, vol. 83, pp. 6, 2003.

[30] M. B. Viani, T. E. Schaffer and A. Chand, "Small cantilevers for force spectroscopy of single molecules," *Journal of Applied Physics*, vol. 86, pp. 2258, 1999.

[31] M. B. Viani, T. E. Schaffer, G. T. Paloczi, L. I. Pietrasanta, B. L. Smith, J. B. Thompson, M. Ritchie, M. Rief, H. E. Gaub, K. W. Plaxco, A. N. Cleland, H. G. Hansma and P. K. Hansma, "Fast imaging and fast force spectroscopy of single biopolymers with a new atomic force microscope designed for small cantilevers," *Review of Scientific Instruments*, vol. 70, pp. 4300, 1999.

[32] G. Schitter, K.J. Astrom, B.E. DeMartini, P.J. Thurner, K.L. Turner, and P.K. Hansma, , "Fast imaging and fast force spectroscopy of single biopolymers with a new atomic force microscope designed for small cantilevers," *Review of Scientific Instruments*, vol. 15, pp. 906-915, 1999.

[33] S. Devasia, E. Eleftheriou, and S. O. R. Moheimani, "A survey of control issues in nanopositioning," *IEEE Trans. on Control Systems Technology*, vol. 15, pp. 802, 2007.

[34] Q. Zou and S. Devasia, "Preview-based optimal inversion for output tracking: Application to scanning tunneling microscopy," *Control Systems Technology*, vol. 12, pp. 375–386, 2004.

[35] Q. Zou, K. K. Leang, E. Sadoun, M. J. Reed, and S. Devasia, "Control Issues in High-speed AFM for Biological Applications: Collagen Imaging Example," *Special Issue on "Advances in Nano-technology Control", Asian Journal Control*, vol. 8, pp. 164, 2004.

[36] D. Abramovitch, S. Andersson, L. Pao, and G. Schitter, "A tutorial on the control of atomic force microscope," *Proceedings of American Control Conference*, pp. 3499–3502, New York City, NY, July 2004.

[37] Y. Wu, Q. Zou and C. Su, "A current cycle feedback iterative learning control approach to AFM imaging," *Proceedings of American Control Conference*, vol. 15, pp. 2040-2045, Seattle, WA, June 2007.

[38] A. A. Tseng, A. Notargiacomo, and T. P. Chen, "Nanofabrication by scanning probe microscope lithography: A review," *Journal of Vacuum Science & Technology B: Microelectronics and Nanometer*, vol. 23, pp. 877–894, May, 2005.

[39] A. Chimmalgi, C. P. Grigoropoulos, and K. Komvopoulos, "Surface nanostructuring by nano-/femtosecond laser-assisted scanning force microscopy," *Applied Physics*, vol. 97, p. 104319, 2005.

[40] Z. Xu, K. Kim, Q. Zou, and P. Shrotriya, "Broadband measurement of rate-dependent viscoelasticity at nanoscale using scanning probe microscope: Poly (dimethylsiloxane) example," *Applied Physics Letters*, Vol. 93, pp. 133103–133105, 2008.

[41] T. C. Waite, Q. Zou, and A. Kelkar, "Inversion-based feedforward approach to broadband acoustic noise reduction," *Journal of Vibration and Acoustics*, vol. 130, p. 051010, October, 2008.

[42] A. C. Shegaonkar and S. M. Salapaka, "Feedback based simultaneous correction of imaging artifacts due to geometrical and mechanical cross-talk and tip-sample stick in atomic force microscopy," *Review of Scientific Instrument*, vol. 78, p. 103706, 2007.

[43] *Ä*. Hoffmann, T. Jungk, and E. Soergel, "Cross-talk correction in atomic force microscopy," *Review of Scientific Instrument*, vol. 78, p. 016101, 2007.

[44] L. Y. Pao, J. A. Butterworth, and D. Y. Abramovitch, "Combined feedforward/feedback control of atomic force microscopes," in *acc*, (New York City, USA), pp. 3509-3515, July 2007.

[45] T.-H. Fang and W.-J. Chang, "Effects of afm-based nanomachining process on aluminum surface," *Journal of Physics and Chemistry of Solids*, vol. 64, pp. 913-918, 2003.

[46] A. Notargiacomo, V. Foglietti, E. Cianci, G. Capellini, M. F. Adami, P. Evangelisti, and C. Nicolin, "Atomic force microscopy lithography as a nanodevice development technique," *Nanotechnology*, vol. 10, p. 458, 1999.

VITA

Yan Yan was born in Xi'an, China. She obtained her bachelor degree in Automatic Control from Northwestern Polytechnic University, Xi'an, China in 2007. In 2009, she earned her Master of Science in Mechanical Engineering at Iowa State University.